

1 The protocataclasite dilemma: *in situ* ³⁶Cl and REE-Y lessons from an impure limestone
2 fault scarp at Sparta, Greece

3 ~~Paleoearthquake reconstruction on an impure limestone fault scarp at Sparta, Greece~~

4
5 Bradley W. Goodfellow^{1,2,3,4}, Marc W. Caffee^{5,6}, Greg Chmiel⁵, Ruben Fritzon^{1,3#}, Alasdair
6 Skelton^{2,3}, Arjen P. Stroeven^{1,3*}

7
8 ¹Department of Physical Geography, Stockholm University, Stockholm, Sweden

9 ²Department of Geological Sciences, Stockholm University, Stockholm, Sweden

10 ³Bolin Centre for Climate Research, Stockholm University, Stockholm, Sweden

11 ⁴Geological Survey of Sweden, Killiansgatan 10, Lund, Sweden

12 ⁵Department of Physics and Astronomy/Purdue Rare Isotope Measurement Laboratory,
13 Purdue University, West Lafayette, USA

14 ⁶Department of Earth, Atmospheric, and Planetary Sciences, Purdue University, West
15 Lafayette, USA

16
17 *Corresponding author

18 Email: arjen.stroeven@natgeo.su.se

19 Phone: +46(0)8-16 4230

20 #Now at Celsiusskolan, Sporthallsvägen 7, 828 33 Edsbyn, Sweden

21
22
23 **Abstract**

24
25 Reconstructions of paleoseismicity are useful for understanding, and mitigating, seismic
26 hazard risks. We apply cosmogenic ³⁶Cl exposure-age dating and concentrations of rare-earth
27 elements and yttrium (REE-Y) to the paleoseismic history of the Sparta fault, Greece.
28 Bayesian-inference Markov chain Monte Carlo modeling of ³⁶Cl concentrations along a 7.2
29 m-long vertical profile on the Sparta Fault scarp at Anogia indicate an increase in average
30 slip rate of the scarp from 0.8–0.9 mm yr⁻¹ at 6.5–7.7 kyr ago to 1.1–1.2 mm yr⁻¹ up to the
31 devastating 464 B.C.E. earthquake. Average exhumation of the entire scarp up to the present
32 day is 0.7–0.8 mm yr⁻¹. Modelling does not indicate additional recent exhumation of the
33 Sparta fault after 464 B.C.E. The Sparta fault scarp is composed of fault breccia, containing
34 quartz and clay-lined pores, in addition to host rock-derived clasts of calcite and
35 microcrystalline calcite cement. The impurities control the distribution of REE-Y in the fault
36 scarp and contribute spatial variation to ³⁶Cl concentrations, which precludes the
37 identification of individual earthquakes that have exhumed the Sparta fault scarp from either

38 of these data sets. REE-Y may illustrate processes that localize slip to a discrete fault plane in
39 the Earth's near-surface but their potential use in paleoseismicity would benefit from further
40 evaluation. Reliable rReconstructions of paleoseismicity are useful for understanding, and
41 mitigating, seismic hazard risks. In this study, wWe apply cosmogenic ^{36}Cl exposure age
42 dating and concentrations of rare earth elements and yttrium (REY) to unravelling the
43 paleoseismic history of the Sparta fault, Greece, which is a range bounding normal fault
44 developed in limestone. 6.5 additional recent after the event. emay exemplify behavior
45 observed Modeling of ^{36}Cl concentrations along two vertical profiles on the Sparta Fault
46 indicates a clustering of four earthquakes within a 1.5 kyr period that culminated with the 464
47 B.C.E. event that devastated Spartan society. Cumulative uplift was as high as 2.8 mm yr^{-1}
48 during that period, compared with $\sim 0.6\text{--}0.9 \text{ mm a}^{-1}$ over the preceding 2.7–4.4 kyr. Because
49 earthquake activity may shift between faults in extensional settings, a large magnitude
50 earthquake is not necessarily indicated as being overdue by the present ~ 2.5 kyr quiescent
51 period. More generally, accurate identification of individual earthquakes is presently
52 constrained by spatial variations in ^{36}Cl concentration profiles that reflect neither exposure
53 duration nor imprints of former soil profiles. In cases where this is attributable to
54 mineralogical variations, such as in the Sparta fault scarp, present chemical preparation
55 techniques for AMS measurement of ^{36}Cl may insufficiently account for those variations.
56
57 The Sparta fault scarp is composed of fault breccia, which contains quartz and clay lined
58 pores, in addition to host rock derived clasts of calcite and microcrystalline calcite cement.
59 Iare potentially identified within vertical , variations occurring as a result of exposure
60 duration Mwhich occur overprint scatter in concentrations that not be accounted for TThe
61 exchange of REY between the hanging wall colluvium and the fault scarp calcite, which has
62 also been applied to the study of paleoseismicity on other limestone normal faults, ; on the

63 ~~Sparta fault it is overwhelmed on this fault scarp by REY attached to the breccia pore clays.~~
64 ~~Holocene earthquakes and their magnitudes, inferred from fault slip lengths, therefore cannot~~
65 ~~be inferred from REY data for impure limestone faults such as the Sparta fault but may,~~
66 ~~rather, these data may indicate processes of fault evolution in the Earth's near surface.~~

67

68

69 **Keywords**

70 ³⁶Cl exposure dating; earthquake; limestone; normal fault; ~~REY~~REE-Y elements; Sparta fault

71

72 **1 Introduction**

73

74 Seismic hazard risks are significant in many parts of the world and studying the magnitude,
75 recurrence, mechanisms, and impacts of past earthquakes helps form a basis for mitigating
76 current and future risk. While historical earthquake records are a crucial archive (Gürpınar,
77 2005), their spatial distribution is patchy and the recurrence interval of large earthquakes on
78 many faults ~~exceeds predates~~ historical records ~~s-lengths~~. Geologic-based Paleoseismic studies
79 that use geologic evidence to iinferences regarding past earthquakes, and even potentially
80 unravel key earthquake characteristics, such aearthquake timing, recurrence intervals, and
81 the magnitudes of slip and shaking intensity, are ~~therefore~~ an essential component of seismic
82 hazard risk mitigation (McCalpin, 2009, p. 24). Topographic expressions of tectonic faults,
83 the displacement of surficial sediments revealed in trenches, and geochemical alterations on
84 subaerially exposed fault surfaces, may each provide evidence useful to the study of
85 paleoseismicity (e.g., Benedetti et al., 2002; Dramis and Blumetti, 2005; Michetti et al., 2005;
86 Carcaillet et al., 2008; Manighetti et al., 2010; Mouslopoulou et al., 2011; Smith et al., 2014;
87 Cowie et al., 2017; Mozafari et al., 2022). ~~In this study we use~~ Here we apply concentrations

88 of cosmic-ray-produced (cosmogenic) ^{36}Cl and concentrations of rare-earth elements and
89 yttrium (REYREE-Y) to study the paleoseismic history of paleoseismicity on the Sparta fault
90 at Anogia, Greece (Fig. 1a, b).

91

92 The Mediterranean is a densely populated seismically active region ~~that was~~ subjected to
93 7360 earthquakes of magnitude (M) > 4 during 1998–2010 (Godey et al., 2013). Within the
94 Aegean tectonic plate (Fig. 1a), and around its margins, there were >1450 ~~such~~ earthquakes
95 during this period, 77 of which were $M > 5$. In central Greece, earthquakes are associated
96 with normal faults, which occur because of extension of the Aegean plate (Jolivet et al.,
97 2013). In limestone, they may be identified by spectacular scarps, which form from the
98 accumulation of bedrock slip that occurs during successive earthquakes. Holocene fault
99 scarps can be well-preserved (Armijo et al., 1991), ~~which makeings~~ them ~~potentially~~ suitable
100 targets for paleoseismic studies.

101

102

103 Paleoseismic information has been derived for limestone normal faults from The
104 concentrations of *in situ* produced cosmogenic ^{36}Cl (Zreda and Noller, 1998; Mitchell et al.,
105 2001; Benedetti et al., 2002; Palumbo et al., 2004; Schlagenhauf et al., 2010; Tesson et al.,
106 2016; Cowie et al., 2017; Iezzi et al., 2021; Mozafari et al., 2022) has been used to infer
107 paleoseismic activity in limestone normal faults. This nuclide is produced from spallogenic
108 and muonic reactions that occurring in ^{40}Ca when limestone is exposed to cosmogenic
109 radiation. Following an earthquake, the newly exposed scarp segment is exposed the
110 secondaries from cosmic radiation and accumulates ^{36}Cl , the concentration of which is
111 dependent upon the duration of subaerial exposure, thereby potentially allowing the
112 earthquake to be dated. However, These However, because earthquakes may be closely

113 clustered in time (Bubeck et al., 2015) and the measured ^{36}Cl concentrations can be fit may be
114 consistent with a range of models (Goodall et al., 2021); a unique unequivocal fit to a single
115 model may not be possible. , both of which can challenge the identification of individual
116 earthquakes that generate slip on a fault scarp. Accurately identifying individual earthquakes
117 is further challenged by ^{36}Cl concentrations along vertical profiles that deviate from the
118 simple step-wise patterns theoretically predicted patterns. by step-wise exhumation of
119 fault scarps. Indeed, such These deviations appear to be a ubiquitous feature of normal faults
120 developed in limestone (e.g., Benedetti et al., 2002; Palumbo et al., 2004; Tesson et al., 2016;
121 Cowie et al., 2017; Goodall et al., 2021; Mozafari et al., 2022; Dawood et al., 2024).
122 Collectively, these challenges have driven the development of more sophisticated models to
123 support paleoseismic inferences from ^{36}Cl concentration profiles, including the timing and
124 slip magnitudes of earthquakes; for example . Recently, these models have incorporated
125 Bayesian modeling incorporates inferences from prior geologic information (Cowie et al.,
126 2017; Beck et al., 2018; Tesson and Benedetti, 2019; Tikhomirov et al., 2019; Goodall et al.,
127 2021, Iezzi et al., 2021) with the goal of making more robust inferences about past tectonic
128 activity.

129
130 Fault scarps may be exhumed by earthquakes clustered within several thousands of years and
131 then lie dormant for similar, or even longer, periods (Wallace, 1987; Friedrich et al., 2003;
132 Benedetti et al., 2013, Cowie et al., 2017). Whereas Although this complicates interpretations
133 the determination of earthquake recurrence intervals, periods of earthquake clusters
134 and followed by intervening quiescence may be interpreted from variations in slip rate may be
135 identifiable discerned from fault scarp ^{36}Cl concentrations (Goodall et al., 2021). Exposure
136 ages from of faults extending over the Holocene faults may can therefore provide information

137 essential to determining the seismogenic potential of a fault (Tesson et al., 2016), even where
138 individual earthquakes cannot easily be determined.
139
140 Measurements of REE-Y elements have also been used to unravel paleoseismic information
141 on limestone fault scarps, frequently together with ³⁶Cl dating (Carcaillet et al., 2008;
142 Manighetti et al., 2010; Mouslopoulou et al., 2011; Tesson et al., 2016; Bello et al., 2023;
143 Moraetis et al., 2023). This is because tThe distribution of REE-Y elements vertically along
144 fault scarps may indicate imprints of result from exchanges with former hanging-wall soil
145 REE-Y that have been before uplifted by successive earthquakes. According to this model
146 (Carcaillet et al., 2008; Bello et al., 2023; Moraetis et al., 2023), REE-Y are would be leached
147 from subaerially exposed scarp surfaces through calcite dissolution and accumulate in the
148 surfaces of the hanging wall soil where they form organic complexes (Carcaillet et al., 2008;
149 Bello et al., 2023; Moraetis et al., 2023). Because of low pH, calcite dissolution is highest
150 where the soil surface contacts abuts the scarp surface and the REE-Y may becomes locally
151 enriched in the adjacent scarp surface through soil-to-scarp REE-Y exchange during
152 reprecipitation of calcite. In this model P Peaks in REE-Y on fault scarp surfaces that are now
153 subaerially exposed may therefore represent former soil surfaces, which are now exposed to
154 leaching and subsequent accumulation in the hanging wall soil, thus completing a cycle. pthe
155 subaerially a means to infer displacement relative to current, and leach, resulting in a new
156 cycle of an older soil contact point on the hanging wallThe spacing of these REE-Y peaks
157 may permit paleoseismic inferences such as the identification of the number of slip events
158 and the, vertical displacement lengths, and earthquake magnitudes. These inferences can be
159 made independently of ³⁶Cl measurements. Using both techniques could provide robust
160 paleoseismic information for seismic risk assessment models. which may help to verify and
161 strengthen interpretations of past earthquakes using this nuclide.

162
163
164
165
166
167
168
169
170
171
172
173
174
175
176
177
178
179

~~Earthquakes inferred from incremental slips of limestone normal faults have been dated with concentrations of *in situ* produced cosmogenic ^{36}Cl (Zreda and Noller, 1998; Mitchell et al., 2001; Benedetti et al., 2002; Palumbo et al., 2004; Schlagenhauf et al., 2010; Tesson et al., 2016; Cowie et al., 2017; Mozafari et al., 2022). This nuclide is produced from spallogenic and muonic reactions that occur in ^{40}Ca when limestone is exposed to cosmogenic radiation. Following an earthquake, the newly exposed scarp segment accumulates ^{36}Cl , the concentration of which is dependent upon the duration of subaerial exposure, thereby potentially allowing the earthquake to be dated. More recently, ^{36}Cl dating has been complemented with measurements of REY because their distribution vertically along fault scarps may indicate imprints of former hanging wall soil REY that have been uplifted by successive earthquakes (Carcaillet et al., 2008; Manighetti et al., 2010; Mouslopoulou et al., 2011; Moraetis et al., 2015). Peaks in REY may represent former soil surfaces and their spacing may permit paleoseismic inferences such as the number of slip events, vertical displacement lengths, and earthquake magnitudes. These inferences can be made independently of ^{36}Cl measurements, which can help to verify and strengthen interpretations of past earthquakes using this nuclide.~~

~~A~~The pioneering cosmogenic ^{36}Cl study of the Sparta fault by Benedetti et al. (2002) ~~guided~~ our interest because motivated our studies. Benedetti et al. ~~they~~ found evidence at Parori (Fig. 1b) for the historically recorded 464 B.C.E. earthquake that destroyed Sparta (Armijo et al., 1991); and ~~inferred an additional~~ five older earthquakes. ~~However~~ Interestingly, they were unable to ~~date~~ substantiate a displacement from the historical 464 B.C.E. earthquake slip at nearby Anogia. Our study objectives were to: (i) study slip rates on the Sparta fault at Anogia, by taking advantage of recent advances in both the measurement of ^{36}Cl and

187 earthquake modelling, that accounting for all ^{36}Cl production pathways and shielding effects
188 (Schlagenhauf et al., 2010), and Bayesian modelling using prior knowledge such as the 464
189 B.C.E. earthquake through Bayesian inference (Goodall et al., 2021); (ii) Complement the
190 ^{36}Cl exposure dating with measurements of REE-Y to best constrain the paleoseismic history
191 of this fault.

192 ~~A pioneering cosmogenic ^{36}Cl study of the Sparta fault by Benedetti et al. (2002) guided our~~
193 ~~interest because they found evidence at Parori (Fig. 1b) for the historically recorded 464~~
194 ~~B.C.E. earthquake that destroyed Sparta (Armijo et al., 1991), and inferred an additional five~~
195 ~~older earthquakes. However, they were unable to date the historical slip at nearby Anogia.~~
196 ~~Our study objectives were to: (i) Re-date the paleoseismicity of the Sparta fault at Anogia, to~~
197 ~~test for the surprising absence of the 464 B.C.E. earthquake, by taking advantage of recent~~
198 ~~advances in both the measurement of ^{36}Cl and earthquake modelling that accounts for all ^{36}Cl~~
199 ~~production pathways and shielding effects (Schlagenhauf et al., 2010), and; (ii) Complement~~
200 ~~the ^{36}Cl dating with measurement of REY to best constrain the paleoseismic history of this~~
201 ~~fault.~~

202

203 **2 Geological Setting**

204

205 The Sparta fault is a 64 km long, NNW–SSE striking, range-bounding normal fault in
206 southern Peloponnese (Fig. 1a, b). It separates the eastern flank of the Taygetos Mountains
207 (maximum elevation of 2407 m a.s.l.) from the Sparta Basin (Fig. 1b). The Sparta fault is part
208 of a larger normal fault system, which exceeds 150 km in length, and is matched on the
209 western margin of the Taygetos Mountains by the antithetical Kalamata fault and other
210 similar faults located offshore of the Mani Peninsula (Fig. 1a; Armijo et al., 1991). The
211 subaerially exposed scarp of the Sparta fault is developed in late Senonian-Eocene limestones

212 of the Ionian unit (Institute for Geology and Subsurface Research, 1969; Armijo et al., 1991).
213 Folded and tilted Permian to early Triassic pelitic and psammitic sedimentary and
214 metasedimentary units outcrop in the Taygetos Mountains and are also offset by the Sparta
215 fault at depth (Institute for Geology and Subsurface Research, 1969; Armijo et al., 1991).
216 Geomorphic evidence for Quaternary uplift along the eastern flank of the Taygetos
217 Mountains includes steep triangular facets (20° – 40°) that are hundreds of meters high along
218 the central portion of the range and decrease in height towards the N and S, wineglass
219 canyons, perched valleys, and alluvial fans having up to 4 m of entrenchment near the Sparta
220 fault trace (Armijo et al., 1991; Benedetti et al., 2002; Pope and Wilkinson, 2005;
221 Papanikolaou et al., 2013). Collectively, the evidence indicates ~~a tectonically active an~~
222 environment that has been tectonically active during the Holocene.

223
224 The Sparta fault scarp is nearly continuous along strike and it reaches a maximum height of
225 10–12 m in its central portion but tapers towards both ends. Hanging wall erosion associated
226 with stream incision can locally form higher scarp segments. The scarp has a ~~65° – 68~~ 61 – 64°
227 dip and, in all but a few locations, slickensides have been eroded away following
228 exhumation. The slope of the hanging wall ground surface matches that upslope of the
229 footwall, which indicates a contiguous hillslope prior to formation of the present scarp and
230 that sediment accumulation at the scarp base is generally minor. ~~However, Some~~ wedges of
231 sediment are locally present on the hanging wall and in some places are welded to the scarp
232 face, in positions now perched above the hanging wall (Fig. S1). These wedges may have
233 been perched by earthquake-induced displacement on the Sparta fault or are debris deposits
234 from mass movements that have partly eroded. It is possible that other sediment wedges were
235 also formerly attached to the scarp face but have since fallen off.

236

237 Our sampling site is located at Anogia, where the Sparta fault scarp is 6.8 m high (Fig. 1c),
238 sparsely fractured, and displays a smooth surface texture (Fig. 1d-e). Apparent slickensides
239 are faintly -traces are- visible as grooves that may have been widened and deepened by
240 weathering, and the surface displays a black coating, like those commonly occurring on
241 limestone and which contain higher concentrations of SiO₂ and Al₂O₃ than the underlying
242 rock (Carcaillet et al., 2008). The scarp surface at Anogia also displays a spatially variable
243 distribution of subaerial weathering features such as rills and dissolution pits, which we
244 avoided in our sampling. The lower-angle hillslopes on both the foot wall (above the fault
245 scarp) and hanging wall display a patchy distribution of ~~frequent~~ bedrock outcrops and an
246 indurated allochthonous regolith composed of limestone clasts, with a matrix of red aeolian
247 dust and calcite cement. An outcrop of limestone about 50 m upslope of the fault scarp
248 reveals folded and tilted bedding. The bedding nearest to the scarp has a dip of 45–60° and a
249 strike of 268–279°, which corresponds with those for the fault scarp, indicating that faulting
250 appears to exploit these structural weaknesses in the bedrock. In contrast to Benedetti et al.
251 (2002) we did not neither observed scarps with a total offset of 2–3 m within tens of
252 meters downslope of the Sparta fault scarp (Benedetti et al., 2002). Neither did we observe,
253 nor observed fault scarps within hundreds of meters upslope of the Sparta fault scarp. If
254 earthquakes, including at 464 B.C.E. B.C.E., bypassed the fault scarp at Anogia (Benedetti et
255 al., 2002), they did not leave geomorphic expressions that we could be observed on field
256 reconnaissance.

257

258

259 **3 Methods**

260

261 To study the paleoseismicity of the Sparta fault, we combined Accelerated Mass
262 Spectrometry (AMS) measurements of cosmogenic ^{36}Cl concentrations from samples
263 collected from the Sparta fault scarp with field and laboratory analyses of scarp composition
264 and mineralogy, and with field measurements of hanging wall soil composition and pH. We
265 made these measurements by sampling a vertical ^{36}Cl profile at Anogia, upwards from the
266 ground surface and adjacent to the sampling transect of Benedetti et al. (2002) for direct
267 comparison with that pre-existing record (Fig. 1c). We also took samples for ^{36}Cl and
268 mineralogical analyses, including ~~REYREE-Y~~, from a second vertical profile located about
269 50 m to the south (Fig. 1c). We chose this additional site for its smooth, non-fractured, fault
270 scarp surface, and sampling was completed from the top of the scarp to 80 cm below the
271 present ground surface, following hand excavation of a pit.

272

273 **3.1 ^{36}Cl concentrations**

274 We sampled the first profile (Anogia A), adjacent to the southern margin of the Benedetti et
275 al. (2002) profile, for ^{36}Cl by using an angle grinder to cut $10*20*~~32.5~~$ cm ($h*w*d$) slabs
276 from the ground surface to a height of 3.9 m (Fig. 1c, d). Because of a crack in the fault scarp
277 at 1.1 m above the ground, the transect was shifted ~~sideways~~-laterally (towards the north) by
278 40 cm, thus duplicating the measurement at 1.1 m. A total of 37 samples from this profile
279 were measured for ^{36}Cl concentration. We sampled the second profile (Anogia B), ~ 50 m
280 further to the south, for ^{36}Cl and mineralogical analyses initially by drilling 14 cores of 4 cm
281 diameter to a depth of 3 cm into the scarp surface (Fig. 1c, e). Four of these cores were
282 spaced at 20 cm intervals below the ground surface and eight were spaced at 80 cm intervals
283 above the ground surface to a height of 6.4 m, which is 0.4 m below the top of the scarp.
284 These samples were augmented by another two drill core samples at 1.2 m and at 6.0 m.
285 Subsequently, we took 20 samples from this profile using an angle grinder to cut $10*20*~~2.53~~$

286 cm ($h*w*d$) slabs from the ground surface to a height of 2.0 m (Fig. 1c). A total of 71
287 samples from the three profiles were subjected to preparation chemistry for ^{36}Cl targets and
288 measured using AMS.

289
290 For ^{36}Cl measurements, limestone samples were crushed to approximately 0.5 mm diameter
291 and the whole sample was used without removing any size fraction through sieving. Prior to
292 partial dissolution approximately 120 g of crushed material was washed with deionized water
293 to remove fines. Following Stone et al. (1996), meteoric ^{36}Cl was removed using two cycles
294 of partial dissolution with nitric acid to dissolve 5% (by mass) of the carbonate each time. To
295 prepare the AMS target we used 30 g of dried sample, spiked with 1 mg of ^{35}Cl -enriched
296 sodium chloride carrier (Source: Icon Isotopes, ^{35}Cl 99.635 atom %, $^{35}\text{Cl}/^{37}\text{Cl} = 273$) to
297 measure native chloride by isotope dilution. A slurry of the sample and 120 g of deionized
298 water was slowly dissolved with 60 g of concentrated trace-metal grade nitric acid. Post-
299 dissolution, both liquid and undissolved solids were quantitatively transferred to a centrifuge
300 bottle where the solids were removed by centrifugation. The supernatant was decanted to
301 another centrifuge bottle and chloride was precipitated using one molar silver nitrate. After a
302 settling period, the bottle was centrifuged to isolate the silver chloride which was then
303 washed, dissolved with ammonium hydroxide, and treated with barium nitrate to remove
304 sulfate in preparation for further purification by chromatography. The solution was loaded
305 onto 5 ml of Bio-Rad AG 1-X8 strong anion-exchange resin and chloride was moved through
306 with 0.50 mmol, and then 0.150 mmol, nitric acid. After re-precipitation with silver nitrate
307 and a washing step the silver chloride was dried and packed into silver bromide-cored copper
308 holders. AMS measurements were performed at the Purdue Rare Isotope Measurement
309 Laboratory according to procedures in Muzikar et al. (2003); standards used for the
310 measurement are described in Sharma et al. (1990).

311

312 3.1.1 Bayesian modelling of ^{36}Cl concentrations

313 ~~To do this we used a~~We apply the Bayesian inference Markov chain Monte Carlo (MCMC)
314 ~~code from~~ Goodall et al. (2021) to identify slip rates from ^{36}Cl concentrations. ~~This Matlab~~
315 ~~code~~MCMC builds upon ‘modelscarp’ from Schlagenhauf et al. (2010), which models the
316 number of earthquakes, their ages, and resulting displacements from ^{36}Cl concentrations
317 based on user-defined inputs. ‘Modelscarp’ accounts for each ^{36}Cl production pathway in
318 limestone (Table 1 in Schlagenhauf et al., 2010). The Goodall et al. (2021) MCMC code is
319 adapted from Cowie et al. (2017) to generate potential slip histories.

320

321 ~~The parameters analyzed by t~~The MCMC code to define a slip history
322 ~~including~~models: (i) ~~the~~ scarp age, which is the timing of the earthquake to exhume
323 the uppermost, and therefore oldest, part of the fault scarp; (ii) ~~the~~ time at which each
324 subsequent earthquake occurred and the corresponding height of exhumed scarp, and; (iii) ~~the~~
325 time since the most recent earthquake exhumed the lowest part of the fault scarp (elapsed
326 time), ~~which exhumed the lowermost part of the fault scarp. Because there is no attempt to~~
327 ~~identify individual earthquakes, t~~The exhumation of the entire scarp is attributed to a user-
328 defined number of earthquakes that each exhumed the same vertical length of scarp. The
329 timing of each earthquake, apart from the first and last, is ~~therefore also influenced~~
330 ~~by~~dependent on the selected number of earthquakes. ~~Because of our focus on slip rates,~~
331 ~~we~~We follow Goodall et al. (2021) in using the flexible change point method of Cowie et al.
332 (2017), ~~which in our application allows the timing in~~for variable slip rates to vary between
333 iterations.

334

335 We parametrized the Goodall et al. (2021) MCMC model as follows. (i) We defined the scarp
336 age as 8000 years with a 1σ normally distributed prior of 1500 years. This selection is partly
337 based on the presumption record that presently visible contemporary faults scarps in the
338 Mediterranean region are Holocene in age. They have been exhumed since the last glacial
339 maximum (LGM) because hillslope bedrock erosion and regolith transport rates were much
340 higher ~~are much lower than today~~ during the LGM (e.g., more than ten times higher for the
341 Magnola Fault in Italy; Tucker et al., 2011), ~~when high rates of slope erosion and regolith~~
342 ~~transport prevented~~ ruptured fault scarps from persisting as subaerially exposed features
343 (e.g., Benedetti et al., 2002; Cowie et al., 2017; Goodall et al., 2021). ~~Post-LGM erosion and~~
344 ~~transport rates are, for example, more than 10x lower than LGM rates for the Magnola Fault,~~
345 ~~Italy (Tucker et al., 2011). The selection of 8000 years adopted scarp age is refined through~~
346 ~~a consequence of fitting a modelled ^{36}Cl concentration profile to the measured ^{36}Cl~~
347 ~~concentrations profile using the ‘modelscarp’ code embedded in the MCMC model of~~
348 ~~Goodall et al. (2021) of MCMC. The scarp age is also balanced by the period of pre-~~
349 ~~exposure procedure modification the prior, which is the translates to as the ^{36}Cl inventory that~~
350 ~~accumulated in the highest part of the scarp in the that accumulated in the bedrock while it was~~
351 ~~mantled by a up to a few meters of colluvium prior to before first initial post-LGM subaerial~~
352 ~~exposure accrued underneath~~ A wide Gaussian prior (5000–16 000 years), is assigned in our
353 modeling to account for the uncertainty in scarp age. (ii) ~~The~~ The time since the most recent
354 earthquake Elapsed time is defined as 2500 years, based on the youngest known earthquake
355 on the Sparta Fault of 464 B.C.E. B.C.E. event ~~and the absence of any historical record of a~~
356 ~~more recent earthquake on the Sparta Fault. However, we~~ We assign a 1σ uncertainty of 1000
357 years ~~to this elapsed time~~ to reflect uncertainty in the historical record. (iii) To further define
358 the most likely slip rate history for the Sparta fault ~~averaged over time and scarp length, we~~
359 completed multiple model runs ~~where we varied~~ with varying the number of earthquakes

360 ~~between three and seven (three to six) and the ³⁶Cl spallation production rates between end-~~
361 ~~member values of (48.8 ± 3.5 to 59.4 ± 4.3 atoms g Ca⁻¹ yr⁻¹).~~ These end-member production
362 rates are ~~recalculated~~ from Stone et al. (1996) and Schlagenhauf et al. (2010) calculated from
363 ~~Lifton et al., (2005), respectively, by al., respectively.~~ All model runs used the temporally
364 variable geomagnetic field ~~from~~ of Lifton et al. (2005) to scale the ³⁶Cl spallation production
365 rate and spallation production rates for K, Ti, and Fe are as shown in Table 1 from
366 Schlagenhauf et al. (2010). ~~The s~~Scarp age and elapsed time are the priors in the MCMC
367 model, ~~whereas~~ the number of earthquakes defines the timing and location on the scarp of
368 slip change points, ~~and P~~prior probabilities are as defined in the ~~MCMC model code from~~
369 ~~Goodall et al. (2021) MCMC code.~~

370

371 ~~Following Goodall et al (2021), t~~The MCMC algorithm solves for slip rate, including how
372 ~~many times and when it changes. It~~ generates a slip history, using the input parameters
373 conditioned on prior probability, to construct a forward model of ³⁶Cl concentrations for this
374 slip history (Goodall et al., 2021). The ~~proposed~~ quality of the slip history's solution
375 ~~likelihood~~ is then assessed by comparing modelled and measured ³⁶Cl concentration profiles.
376 The algorithm iteratively adjusts a parameter defining the slip history, ~~and recalculating~~ a
377 ~~new the~~ forward model ~~each time~~ solution. Acceptance of the new slip history hinges on
378 ~~either its likelihood surpassing that of the prior model or the ratio of new to current likelihood~~
379 ~~exceeding a randomly selected value from a uniform distribution between zero and one.~~
380 Otherwise, the new model solution is discarded, adhering to the principles of the Metropolis-
381 Hastings algorithm (Metropolis et al., 1953; Hastings, 1970). We ran this process for 200 000
382 iterations, using the parameters in Table 1, and results were assessed on 160 000 iterations
383 after a burn-in phase of 40 000 iterations were excluded to mitigate the influence of initial
384 parameters. ~~We applied a model developed by Schlagenhauf et al. (2010) for the interpretation~~

385 of earthquakes from cosmogenic ^{36}Cl concentrations to the Sparta fault scarp. This model
386 accounts for various parameters that control the ^{36}Cl concentration in a limestone normal
387 fault scarp, including geomagnetic field variations, host rock and hanging wall colluvium
388 chemical compositions and densities, scarp erosion rate, shielding of the scarp base by a
389 colluvial wedge, and the geometries of the fault scarp, the slope above the scarp, and the
390 hanging wall colluvial wedge. Their model uses three statistical parameters, the weighted root
391 mean square (RMSw), the reduced Chi square (χ^2_{red}), and Akaike Information Criterion
392 (AIC) to assess the quality of fit between modelled and measured data to provide an objective
393 assessment of the number, and spatial and temporal spacing, of inferred earthquakes. For our
394 age calculations, we used the sea level high latitude (SLHL) ^{36}Cl production rate from
395 spallation in calcite of $59.4 \text{ atoms g}^{-1} \text{ yr}^{-1}$ and a temporally variable geomagnetic field to scale
396 the ^{36}Cl production rate from Lifton et al. (2005). A more recent ^{36}Cl production rate
397 calibration by Marrero et al. (2016) is not used here because it is scaled using Lifton et al.
398 (2014), which is not included in the model of Schlagenhauf et al. (2010). The Marrero et al.
399 (2016) production rate overlaps with the ^{36}Cl production rate from Lifton et al. (2005), within
400 uncertainty. We complemented the modelling of our new ^{36}Cl results with a re-modelling of
401 the Benedetti et al. (2002) data, using our own data for fault scarp and colluvium
402 composition. Our method of inferring earthquakes was based on fitting ^{36}Cl concentration
403 profiles derived from the Schlagenhauf et al. (2010) model to the actual ^{36}Cl concentration
404 profiles and inferring former soils surfaces from inflection points in the real ^{36}Cl
405 concentration profiles. This allows us to best constrain the paleoseismic history of the Sparta
406 fault over the late Holocene.

409 3.2 Sparta fault scarp composition

410 Fault scarp chemical composition and mineralogy were analyzed from ~~the second sampling~~
411 ~~profile, 50 m to the south of the first sampling profile, Anogia B~~ as follows. An initial
412 elemental analysis was done in the field on the Sparta fault scarp surface using an Olympus
413 Innov-X Delta (40 kV) handheld X-ray fluorescence (XRF) device. This instrument performs
414 elemental analyses with a circular sample spot of 8 mm diameter and can measure elements
415 heavier than Na. All elements lighter than Mg are reported as lighter elements (LE). Of the
416 elements that compose ~~REYREE-Y~~, it was only capable of measuring yttrium. Sampling was
417 done at an interval of 5 cm (or less) over a 7.7 m vertical profile, beginning ~~~90 cm~~04.9 m
418 below the hanging wall soil surface. This profile corresponds with the location of the drill
419 core and 2.0 m-long ^{36}Cl profiles at Anogia B but was measured before either drilling or slab
420 sampling (Fig. 1c).

421

422 For more detailed analyses of elements, including ~~REYREE-Y~~, a total of 39 cores (22 mm
423 and 35 mm diameters and to depths of ~~~4-3~~ cm) were collected every 20 cm from ~~the fault~~
424 ~~scarp-a~~ vertical transect at Anogia B using a portable drill (Fig. 1d). The outermost 1 mm was
425 removed from each core prior to crushing to avoid contamination from the black surface
426 coating. The next 15 mm of each core were then rinsed with cold water, air dried, and
427 crushed using a grinder with a steel mortar to a grain size of $<100\ \mu\text{m}$. This crushing
428 technique might supply additional ~~REYREE-Y~~ to samples (Hickson and Juras, 1986) but if
429 so, this likely occurs systematically across samples and we are more interested in spatial
430 trends, which we confirm independently using the handheld XRF, than absolute abundances.
431 The crushed samples were then analyzed for major and trace elements using fusion
432 inductively coupled plasma mass spectrometry (FUS-ICP-MS) at Activation Laboratories
433 (Ontario, Canada).

434

435 We complemented the FUS-ICP-MS analyses with spot elemental analysis of one rock core
436 from 1.1 m above the scarp base [at Anogia B](#) to make a high-resolution determination of any
437 spatial variations in the scarp composition. This was done with an energy-dispersive X-ray
438 spectroscope (EDS) attached to an environmental scanning electron microscope (ESEM). We
439 used a Quanta FEG 650 with Oxford-Inka EDS, and the analysis was made in a high-vacuum
440 environment at 20 kV. The technique is incapable of detecting [REYREE-Y](#) because their
441 concentrations are too low. Photomicrographs and backscatter images of pore spaces were
442 also taken using the ESEM. These analyses were completed at the Department of Geological
443 Sciences, Stockholm University.

444

445 **3.3 Sparta fault scarp mineralogy**

446 A modal analysis of mineral fractions was completed on thin sections taken from the
447 remaining 38 core samples. This was done by counting 1000 points on each thin section
448 (Hutchison, 1974) using a Pelcon automatic point counter, attached to a Leica (DM LSP)
449 optical microscope. This point counter comprises a stepping frame attached to a control box
450 (power supply) and is also connected to a computer for statistical analyses using Pelcon
451 software version 2. The point counting and mineral identification was made using an
452 objective working distance of 1.52 mm. The line section pre-set step-length was 0.3 mm and
453 the line section distance was 1.5–2 mm. The point counting permitted a detailed quantitative
454 analysis of the mineralogy of the Sparta fault scarp surface. This detailed mineralogy was
455 then compared with the chemical composition data to determine whether phases other than
456 the host limestone are present.

457

458 **3.4 Hanging wall soil chemistry and pH**

459 Soil chemistry and pH were measured in samples taken at ~10 cm intervals to a depth of ~90
460 cm in the pit excavated at the base of ~~the the Sparta fault scarp~~Anogia B profile (Fig. 1c). The
461 elemental analysis was again done with the handheld XRF device. Indicator strips were used
462 to measure pH from mixtures of 1:1 mass ratio of soil:distilled water, and soil:1 M KCl
463 (Sikora and Moore, 2014). These analyses help determine the vertical distribution of
464 REYREE-Y in the soil (using yttrium as a proxy) and indicate how they might correlate with
465 pH and the vertical distribution of REYREE-Y in the fault scarp below the soil surface.

466

467 **4 Results**

468

469 **4.1 Sparta fault ³⁶Cl concentrations**

470 The cosmogenic nuclide ³⁶Cl concentrations from our three profiles (Table S1) and the
471 original Benedetti et al. (2002) ³⁶Cl concentrations are compared in Figure 2. The Anogia A
472 and Anogia B profiles display corresponding trends of increasing ³⁶Cl concentrations with
473 increasing height on the fault scarp. Only at 1.6 m do the trends strongly deviate from each
474 other. The Anogia B profile indicates generally lower ³⁶Cl concentrations including six of 19
475 points that do not overlap within uncertainty ~~of~~with data points at corresponding elevations
476 on the Anogia A profile. Four of those points are located from 1.0 m to 1.3 m. In comparison
477 with Anogia A, the adjacent segment of the Benedetti et al. (2002) profile (0–4 m) shows ³⁶Cl
478 concentrations that are on average 19% higher. Uncertainties (1σ) for data points comprising
479 each profile are almost identical, displaying a mean of 3.8% for the Benedetti et al. (2002)
480 profile versus 3.9% for the Anogia A and Anogia B profiles. However, the Benedetti et al.
481 (2002) profile displays more variation between adjacent sample points than is evident in our
482 profiles. Whereas concentrations differ between the three longest profiles, they show a
483 consistent gradient up to ~4 m on the scarp. Above 4 m on the scarp, both our Anogia B drill-

484 core profile and the Benedetti et al. (2002) profile display matching lower gradients. Whereas
485 differences in measured concentrations between our two profiles and the Benedetti et al.
486 (2002) profile might be expected given technical advances ~~in the 12 to 16 year gap~~ between
487 measurements, successive samples in our data display ~~inconsistent~~ variations ~~that are~~
488 ~~frequently not mirrored~~ between the Anogia A and B profiles, despite them being
489 horizontally separated by only ~ 50 m. ~~This~~This inability to replicate measurements along
490 two adjacent profiles justifies a focus on identifying slip rates using the Goodall et al. (2021)
491 model, rather than individual earthquakes, also because up-scarp ³⁶Cl concentration gradients
492 are more consistent between the profiles.

493
494 Slips rates for the Sparta fault are explored through comparing scarp exhumation generated
495 by three, five, and six modelled earthquakes, where each earthquake exhumes 183 cm, 122
496 cm, and 104 cm, respectively. We focus our analyses on the Anogia A profile supplemented
497 with drill core samples from above 3.9 m on the scarp and from the scarp surface buried by
498 colluvium. This combined profile was chosen for modelling both because the Anogia A
499 profile was sampled at 10 cm intervals up to 3.9 m on the scarp, versus only 2.1 m for Anogia
500 B, and because Anogia A is located adjacent to the Benedetti et al. 2002 profile. Furthermore,
501 MCMC modelling of ³⁶Cl concentrations did not converge with measured concentrations for
502 the full Anogia B profile (i.e., including the drill core samples above 2.1 m), but rather only
503 for the intensively sampled lowermost 2.1 m plus subsurface drill core samples. Modelling
504 only the lowermost 2.1 m plus subsurface drill core samples necessitated changes to scarp
505 age and preexposure from those used for the Anogia A plus drill core sample profile, because
506 this lowermost part of the scarp has a younger age, and to slip length because the 2.1m profile
507 length is indivisible into the 6.5 m length of the Anogia A plus drill core sample profile.
508 These changes, especially to scarp age, invalidate comparisons of slip rates between the two

509 profiles, which are the focus of this paper. We did not measure compositions for the Anogia
510 A samples, so we use a mean scarp composition from Anogia B in our modelling. Results
511 from the Goodall et al. (2001) model applied to the Anogia A plus drill core profile are
512 shown below and in Figure S2, respectively, for end-member ^{36}Cl productions rates of $59.4 \pm$
513 $4.3 \text{ atoms g Ca}^{-1} \text{ yr}^{-1}$ from Schlagenhauf et al. (2010) calculated from Lifton et al., (2005) and
514 $48.8 \pm 3.5 \text{ atoms g Ca}^{-1} \text{ yr}^{-1}$ from Stone et al. (1996). Geochemical data for the fault scarp
515 used in modelling are shown in Table S2. Modelling results from Anogia B (lowermost 2.1 m
516 and subsurface drill core samples and the entire profile) are shown in Figure S3.
517 ~~The cosmogenic nuclide ^{36}Cl concentrations from our three profiles (Table S1) and the~~
518 ~~original Benedetti et al. (2002) ^{36}Cl concentrations are compared in Figure 2. The lowest ^{36}Cl~~
519 ~~concentrations occur in our drill core samples. Whereas age reversals are non-apparent in this~~
520 ~~profile, comprised of widely dispersed sample points, there is a clear decrease in ^{36}Cl with~~
521 ~~depth, including below the soil surface. Our 2.0 m and 3.9 m long profiles display~~
522 ~~corresponding trends with increasing concentrations with increasing height on the fault scarp.~~
523 ~~Only at 1.6 m do the trends strongly deviate from each other. The 2.0 m long profile indicates~~
524 ~~generally lower ^{36}Cl concentrations including six of 19 points that do not overlap within~~
525 ~~uncertainty of data points at corresponding elevations on the 3.9 m long profile. Four of those~~
526 ~~points are located from 1.0 m to 1.3 m. In comparison with our 3.9 m long profile, the~~
527 ~~adjacent segment of the Benedetti et al. (2002) profile shows ^{36}Cl concentrations that are on~~
528 ~~average 19% higher (0–4 m). Uncertainties (1σ) for data points comprising each profile are~~
529 ~~almost identical, displaying a mean of 3.8% for the Benedetti et al. (2002) profile versus~~
530 ~~3.9% for our 3.9 m long and 2.0 m long profiles. However, the Benedetti et al. (2002) profile~~
531 ~~displays more variation between adjacent sample points than is evident in our profiles.~~
532 ~~Whereas concentrations differ between the three longest profiles, they show a consistent~~
533 ~~gradient up to 4 m on the scarp face equivalent to an average uplift rate of $1.0\text{--}1.3 \text{ mm yr}^{-1}$.~~

534 Above 4 m on the scarp, both our drill core profile and the Benedetti et al. (2002) profile
535 display matching lower gradients, which indicates a lower average uplift rate of 0.6–0.9 mm
536 yr⁻¹. If uplift rates are alternatively calculated as occurring prior to the subaerial exposure of
537 the lowermost samples by the most recent earthquake, cumulative uplift rates increase to 2.8
538 mm yr⁻¹ and 1.8 mm yr⁻¹ for the lower parts of the 3.9 m long and Benedetti et al. (2002)
539 profiles, respectively. Both our 2.0 m long and 3.9 m long profiles indicate a local low in
540 ³⁶Cl concentration at ~0.5 m above the ground surface, which is opposite to the Benedetti et
541 al. (2002) profile, where concentrations reach a local high at ~0.5 m. Both of our profiles also
542 display an age reversal at 1.4–1.6 m, which is comparable to the age reversal at 1.2–1.5 m on
543 the Benedetti et al. (2002) profile. Our 3.9 m long profile and the Benedetti et al. (2002)
544 profile each display additional age reversals at 2.6–2.7 m and 3.1–3.2 m on the scarp.
545 Another reversal is also apparent at 3.7–3.9 m in both profiles (including the drill core
546 sample at 4 m). These reversals complement the gradients in being similarities shared by the
547 profiles that are key characteristics for a further analysis of its paleoseismicity using the
548 model of Schlagenhauf et al. (2010).

549

550 The results of the Bayesian inference MCMSMCMC modelling of ³⁶Cl data from the Sparta
551 fault, using the parameters in Table 1, are shown in Figures 3–5. The accepted scarp
552 exhumation models (n = 160 000?) are shown in slip versus time histograms (Fig. 3a). The
553 maximum a posteriori probability (MAP) model, shown by the red line, deviates slightly
554 from the maximum model density (mean model, black line) for each slip segment, but more
555 so for the slip segment at 4.9–6.1 m on the scarp. It indicates three exhumation events
556 between 2.4 and 6.1 m on the scarp, that are closely spaced in time at 5000–6000 years ago.
557 The 95% confidence intervals (Fig. 3b) illustrate little change in variance between model
558 results from lower, younger parts of the scarp to older, higher parts of the scarp, although the

559 MAP model deviates towards being younger than the mean model towards the top of the
560 scarp. The range of accepted models fits the measured ^{36}Cl data well (Fig. 3c) but
561 accommodates a broad range of corresponding slip histories along the entire vertical length of
562 the scarp (Fig. 3d).

563

564 Statistics for how well the MCMC modelling fits the measured ^{36}Cl data and our initial
565 estimates of scarp age (8000 years) and elapsed time (2500 years) ~~since the most recent~~
566 earthquake that exhumed the Sparta fault scarp at Anogia are illustrated in Figure 4 and
567 summarized in Table S2. The posterior probability distribution function indicates that the
568 elapsed time since the most recent earthquake is consistent with the ~~almost 2.5 kyr~~2500-year
569 period following the 464 B.C.E. earthquake (mean of ~~2.54~~254001 \pm 0.15 kyr150-64 years;
570 Fig. 4a). In contrast, the time ~~since~~when the scarp started to ~~be preserved~~form (scarp age),
571 presumably through a decrease in hillslope erosion following the LGM, is indicted by the
572 posterior probability distribution to have been longer than our initial estimate of ~~8 kyr~~8000
573 years (mean of ~~8.81~~8810742 \pm 0.5353002 kyryears; Fig. 4b). Mean values of likelihood, ~~the~~
574 weighted mean root square (RMS_w) and corrected Akaike's Information Criterion
575 (AICc) values are 0.25–0.28, 13.9–14.6, and 863–893, respectively, across the
576 modelled range of the number of slip events (Figs. 4d and 4e; Table S2), indicating that the
577 number of earthquakes (change points) has minor influence on modelling a fit to measured
578 ^{36}Cl concentrations.

579

580 The slip rate for the Sparta Fault is calculated from the most probable of models (i.e., the top
581 6.25% of fits to the ^{36}Cl data ($n = 10\,000$); Fig. 5, Table 2). For the entire vertical length of
582 the fault scarp, and five modelled earthquakes, both the mean and ~~maximum a posteriori~~
583 probability (MAP) slip rates ~~is~~are 0.7–0.8 mm yr⁻¹ for end-member ^{36}Cl production rates,

584 ~~calculated up to the present day (Fig. 5a). For the same calculation but excluding the 2.5~~
585 ~~kyr2500 year since the most recent known earthquake at 464 B.C.E., the slip rates isare~~
586 ~~higher, with a mean and MAP values of 1.1– and 1.2 mm yr⁻¹, respectively (Fig. 5b). The~~
587 ~~lowest 3.7 m of the fault scarp is the most recently exhumed scarp segment and the most~~
588 ~~intensively sampled. It displays a steep ³⁶Cl concentration gradient, which indicates matching~~
589 ~~mean and MAP slip rates of 1.0 mm yr⁻¹, for five model earthquakes (Fig. 5c). The~~
590 ~~upmosthighest 2.5 m of the scarp displays a gentler ³⁶Cl concentration gradient relative to the~~
591 ~~bottom 34.9 m of the scarp isas indicated by our drill core samples and the Benedetti et al.~~
592 ~~(2002) profile to display a gentler ³⁶Cl concentration gradient relative to the bottom 4.9 m of~~
593 ~~the scarp. The mean and MAP slip rates for this scarp segment are consequentlytherefore~~
594 ~~lower, at 0.8–0.9 mm yr⁻¹ (Fig. 5d). Varying the number of earthquakes between three and six~~
595 ~~has minor influence on the calculated slip rates (Table 2). The mean slip rate up to the present~~
596 ~~day varies between 0.7 mm yr⁻¹ and 0.8 mm yr⁻¹ (Fig. 5a) for three to six earthquakes,~~
597 ~~whereas it varies from 1.1 mm yr⁻¹ to 1.2 mm yr⁻¹ up to 464 B.C.E. earthquake (Fig. 5b).~~
598 ~~TheAn increase in mean slip rate occurred during thebetween 6.7 and 5.3 –6.7 kyr period~~
599 ~~(Fig. 5e).~~

600 Using the Schlagenhauf et al. (2010) model, we analyze the number, ages, and magnitudes of
601 earthquakes inferred from a composite ³⁶Cl concentration profile; principally this record
602 contains the 3.9 m profile, but also includes the subsurface samples from our drill core
603 profile, and the drill core samples from 4.1 to 6.4 m (Fig. 3a). The total length of this record
604 then becomes 7.2 m. To match these two data sets, we increase the concentration of each drill
605 core sample by 5%. Integrating these two data sets is necessary to generating fits to the ³⁶Cl
606 data because subsurface data are required by the Schlagenhauf et al. (2010) model. The 5% is
607 chosen to match the ³⁶Cl concentrations in the four drill core samples between 0.8 m and 2.4
608 m with those in the corresponding segments of the 2.0 m and 3.9 m profiles, while

609 maintaining subsurface ^{36}Cl concentrations below those in the samples at 0.1 m on the 2.0 m
610 and 3.9 m profiles. Then, using the same parameters that generated the best model fit to the
611 3.9 m long plus drill core profile (Table 1), we apply the best model fit to our 2.0 m long
612 profile (Fig. 3b) and the Benedetti et al. (2002) profile (Fig. 3c). In both cases, we use the
613 adjusted subsurface data from the drill core profile. For our 2.0 m plus subsurface drill core
614 profile, we used the scarp mineralogy measured for each sample. For the 3.9 m long plus drill
615 core profile and the Benedetti et al. (2002) plus subsurface drill core profile we used a mean
616 composition from our measured scarp mineralogy because we did not determine mineralogies
617 along these profiles. We further compare earthquakes modelled from age reversals in the ^{36}Cl
618 data with earthquakes modelled from potential soil profiles mirrored in scarp geochemistry
619 (REY, SiO_2 and Al_2O_3 ; Fig. 3d). We then use all data to infer the most likely earthquake
620 history for this segment of the Sparta fault.

621
622 From the combined 7.2 m long profile, modelling indicates that five earthquakes at 1.4 m
623 (2.3 kyr B.P.), 2.6 m (2.8 kyr B.P.), 3.9 m (3.2 kyr B.P.), 5.1 m (3.8 kyr B.P.), and 6.5 m (5.9
624 kyr B.P.) provide the best statistical fit to our data (Fig. 3a; Table 1). Our best fit parameters,
625 taken either directly from field measurement or assumed (in the case of ϵ and pre-exposure),
626 are listed in Table 1. The two inferred earthquakes at 1.4 m (2.3 kyr B.P.) and 2.6 m (2.8 kyr
627 B.P.) also provide a good statistical fit to our 2.0 m long profile (Fig. 3b). An inferred five
628 earthquakes on the Benedetti et al. (2002) profile (Fig. 3c) at the same elevations on the scarp
629 as our adjacent composite profile (Fig. 3a) display a statistically weaker fit than obtained for
630 our data (Table 1). Older ages and longer exposure prior to the oldest earthquake (pre-
631 exposure) are necessitated by the systematically higher ^{36}Cl concentrations. Earthquakes
632 inferred from the record of scarp geochemistry (Section 4.3) occur at 0.8 m (1.9 kyr B.P.), 2.6
633 m (2.8 kyr B.P.), 4.0 m (3.0 kyr B.P.), and at 6.4 m (5.9 kyr B.P.) on our 7.2 m long profile

634 (Fig. 3d). Interestingly, this reconstruction has a statistically weaker fit than for earthquakes
635 inferred from reversals in ^{36}Cl concentrations (Fig. 3a; Table 1). We note that for the
636 applicable ^{36}Cl concentration profiles, model fits overestimate ^{36}Cl concentrations at 4 m on
637 the scarp surface (Figs. 3a, c, and d). In Figure 3a, c, and d, an (artificial) earthquake is added
638 to the top of the ^{36}Cl concentration profile to fit all data (Earthquake 1, shown in grey).
639 Because this oldest earthquake is tied to the highest sample on the scarp, without an
640 associated age reversal, and because ^{36}Cl measurements are sparsely spaced above 4 m, the
641 inferred locations on the fault scarp and timing of this earthquake are approximate. We
642 therefore focus our interpretations on the inferred earthquakes lower down on the fault scarp.
643
644 The model fit to our data is sensitive to input parameters, at least two of which are difficult to
645 accurately measure (Fig. 4). It is most sensitive to the scarp dip angle (e.g., a 5° decrease
646 causes the AICc to increase by 12%), followed by the density of colluvium mantling the
647 hanging wall and the rate of scarp surface erosion. It is least sensitive to variations in rock
648 density and hillslope gradient. The colluvium density depends on relative abundances of
649 limestone clasts, mineral soil, organic matter, and water, which vary spatially. Due to, for
650 example, wetting and drying, colluvium density is expected to also vary temporally. Scarp
651 erosion rates remain undetermined. The adopted values for colluvium density and scarp
652 erosion rate are, therefore, those which provide the best model fits to the data. In both cases,
653 those values are also realistic (Table 1). Rock density is prescribed from the literature and
654 colluvium dip, scarp dip, and hillslope gradient are based on measurements. Optimal
655 colluvium and scarp dips are adjusted slightly relative to measured values (i.e., $1-2^\circ$, which is
656 within measurement uncertainty).

657

658 4.2 Granulometry of the Sparta fault scarp surface

659 A first look at the Sparta fault scarp surface yields a misleading impression of homogeneous
660 limestone (Figs. 1, [5a6a](#)), whereas close inspection of the core samples instead reveals a
661 typical fault breccia (Figs. [5b6b-d](#)). This breccia consists of angular-to-rounded limestone
662 clasts with axes of 1–7 mm (in the two-dimensional view provided by thin sections)
663 surrounded by matrix/cement in which clasts are <0.1 mm in length. The fault breccia is
664 defined as a protocataclasite, according to the classification of Woodcock and Mort (2008).
665 The composition of the protocataclasite displays large spatial variations, with some portions
666 containing abundant clasts (Fig. [5e6c](#)), whereas others are dominated by fine matrix (Fig.
667 [5d6d](#)). The proportion of clasts >2 mm ranges from 5% to 20% vertically along the fault
668 scarp and the proportion of matrix ranges from 5% to 60%. We did not measure the thickness
669 of the protocataclasite but it everywhere exceeds the [4-3](#) cm depth of our drill cores.

670

671 **4.3 Sparta fault scarp composition and mineralogy**

672 In addition to a spatially variable granulometry, the fault scarp shows a spatially variable
673 distribution of major and trace elements. The major component is, as expected for limestone,
674 CaO (mean 52.22%) but its concentration varies between 43.83% and 56.64% (Table [S32](#)),
675 which exceeds spatial variations in CaO seen elsewhere in limestone normal fault scarps
676 (Carcaillet et al., 2008; Tesson et al., 2016). Quartz (SiO₂) also occurs, and it too displays
677 spatial variations (0.10%–20.82%), with broad peaks occurring at -0.5–0.4 m [below the](#)
678 [ground](#), [and](#) 0.9–1.2 m, 4.6–4.8 m, and 6.0–6.2 m along the vertical fault scarp profile (Fig.
679 [67](#); Table [S32](#)). An additional peak in SiO₂, but which is not seen in point counting of quartz,
680 occurs at 6.2 m (Fig. [67](#); Tables [S32](#) and [S43](#)). Mean concentrations of other major elements
681 are low in bulk samples, including Al₂O₃ (0.21%), MgO (0.16%), Fe₂O₃ (0.09%), P₂O₅
682 (0.07%), and K₂O (0.05%; Table [S32](#)). However, EDS measurements, such as shown in
683 Figure [7a8a](#), reveal that the concentrations of some elements are frequently much higher in

684 intergranular pores (Fig. 7e8c) than elsewhere in the fault scarp, including Si \leq 38.3%, Al \leq
685 11.7%, Fe \leq 48.4%, and K \leq 7.1% (Table S54). Furthermore, intergranular pores and quartz
686 frequently occur together (Fig. 7b8b) and the concentration of Al₂O₃ covaries with the much
687 more abundant quartz (SiO₂) (Fig. 67).

688

689 Quartz is revealed by microscopy to be present as randomly oriented rounded-to-angular
690 grains that are $<50\ \mu\text{m}$ in diameter (Figs. 5d6d, 7b8b). Quartz is a constituent of the
691 protocataclite fine matrix that is mostly comprised of microcrystalline calcite precipitates
692 and which cements larger host rock-derived CaCO₃ clasts (Figs. 5b6b-d, 7b8b, 8a9a). Point
693 counting further reveals quartz modes ranging from 0.1% to 15.4% of thin section area (Table
694 S43), with higher abundances correlating to higher abundances of fine matrix. The spatial
695 correlations between SiO₂, quartz abundances on point counting, and fine matrix are further
696 ~~indicated-strengthened~~ by ~~the~~-EDS spot elemental ~~analysis-analyses~~ (Fig. 89). Here, the two
697 selected spots in the fine matrix display Si abundances of 29.7% and 28.9%, which contrasts
698 with 1.7% and 0.9% for the two spots located on clasts. CaO abundances display an inverse
699 relationship with SiO₂ (33.7% and 31.2% for the clasts versus 4.8% and 5.1% for the fine
700 matrix). SiO₂ is present largely as quartz, as evidenced by the strong spatial correlation
701 between quartz and SiO₂ along the vertical profile (Fig. 67). Quartz can therefore be used as a
702 proxy for fine matrix abundances in the Sparta fault scarp.

703

704 In addition to the spatial relationship between quartz and fine matrix, we observed in
705 backscatter SEM images that pore spaces, which frequently harbor higher concentrations of
706 Si, Al, K and/or Fe than host rock-derived clasts, are also more abundant in the fine matrix
707 (Fig. 7e8c). These observations provide evidence that clay particles ($< \mu\text{m}$ -scale) frequently

708 coat pore spaces. The abundance of quartz therefore also provides a proxy for the abundance
709 of clay-coated pore spaces.

710

711 Concentrations of ~~yttrium-REE-Y are generally low (1.2–11.1 ppm; Table S5) but~~ vary in a
712 wave-like pattern along the vertical profile, with maxima occurring at -0.4 m, 0.8 m, 2.6 m,
713 4.0 m, and 6.4 m (Y = 1.2–11.1 ppm; Table S6; Fig. 910). These maxima do not
714 systematically decrease with vertical distance above the hanging wall and are not highest in
715 the soil-mantled portion of the scarp. Yttrium (mean 6.3 ppm), La (mean 5.04 ppm), Nd
716 (mean 3.54 ppm), and Ce (mean 2.31 ppm) have the highest concentrations, whereas all other
717 ~~REYREE-Y~~ are <1 ppm (Table S6). The concentrations of ~~REYREE-Y~~ elements co-vary
718 vertically along the scarp surface ($R^2 = 0.95$; Fig. 910a).

719

720 There is no depletion of light (LREE) relative to heavy (HREE) rare-earth elements with
721 increasing height on the subaerially exposed fault scarp, where it ranges between 3.9 and 5.1
722 (Figs. 10b, 11a, Table S6). However, there is a relative depletion of LREE on the scarp
723 surface buried by soil (LREE/HREE is 3.2 to 4.0; Figs. 10b, 11a), with least depletion at 0.-
724 400 cm depth and progressively ~~greater~~larger LREE depletion with increasing depth. Peaks
725 and troughs in the LREE/HREE ratio along the vertical profile ~~do not~~poorly match ~~well~~peaks
726 and troughs in REE-Y concentrations (Figs. 10a, b), although local minima correspond at 3 m
727 and at 5.2 m on the scarp. Accordingly, the correlation between LREE/HREE and total REE-
728 Y concentration is only weak ($R^2 = 0.36$; Fig. 11b). ~~the proportion of light REYREE-Y~~
729 (~~LREYREE-Y~~) to heavy ~~REYREE-Y~~. (HREY) remains constant (ratio ~7:1; Fig. 10; Table
730 S5), and

731

732 REE-Y concentration maxima occur at locations that correspond closely with the Al_2O_3
733 maxima (Fig. 910a; Table S65). Accordingly, ~~there is a strong correlation between~~
734 ~~REY, LREE, HREE, and total REE-Y and are strongly correlated with~~ Al_2O_3 ($R^2 = 0.92$; Figs.
735 11c, S32a). Spatial correlations between ~~REY, REE-Y~~ and SiO_2 ~~and~~ K_2O are also
736 observed ($R^2 = 0.56$ ~~and~~ 0.87 , respectively; Fig. S42c, e). ~~In contrast, the locations of~~
737 ~~REY maxima correlate neither with the location of the present ground surface (-0.4 m) nor~~
738 ~~former ground surfaces at 1.4 m and 5.1 m inferred from ^{36}Cl data. There are, however,~~
739 ~~correlations between REY maxima and former ground surfaces at 2.6 m, 3.9–4.0 m, and at~~
740 ~~6.4–6.5 m modelled from the ^{36}Cl data. Whereas REE-Y concentrations vary in wave-like~~
741 ~~pattern along the scarp, REE-Y is not enriched, and LREE is depleted relative to HREE, in~~
742 ~~the soil-covered scarp surface. In contrast, there is a strong correlation of total REE-Y, LREE~~
743 ~~and HREE with impurities embedded in the scarp that represent quartz sand (SiO_2) and clay~~
744 ~~(Al_2O_3 , SiO_2 , K_2O , and Fe_2O_3). No systematic relationship is therefore apparent between REY~~
745 ~~maxima and either the present soil surface or former soil surfaces inferred from inflection~~
746 ~~points in ^{36}Cl concentrations.~~

747

748 **4.4 Hanging wall soil chemistry and pH**

749 The terra rosa soil mantling the hanging wall primarily comprises aeolian dust (Muhs et al.,
750 2010) and carbonate clasts. At our sample site, the soil thickness at the base of the Sparta
751 fault scarp is 0.8 m and this appears to be stable, at least over the timescale of scarp surface
752 dissolution, as evidenced by a much smoother scarp surface texture below the soil surface
753 compared with the subaerially exposed scarp. Below the organic horizon (~0.1 m thick) the
754 soil is welded, probably by calcite precipitates, and horizons are absent. Soil pH is, in
755 general, slightly acidic along the excavated vertical profile, remaining within a 6.2 to 7.0
756 range (Fig. H12a; Table S76). An outlier occurs at -0.30 m, where the pH is 5.6 ± 0.2 . Soil

757 composition varies with depth (Fig. ~~44b~~12b; Table S87). Concentrations of Si, Al, and K are
758 lower in the organic horizon (11%, 0–5%, and 0.4%, respectively) compared with the
759 remainder of the profile (18%–30%, 5–10%, and 0.5–0.9%, respectively), whereas the
760 concentrations of LE, which includes C, are, as expected, higher in the organic horizon
761 (75%–80%) than in the lower profile segment (51%–64%). The concentration of yttrium
762 ranges from a maximum of 36–39 ppm at -0.5– -0.6 m depth to a minimum of 11 ppm at -0.1
763 m depth and its vertical distribution correlates positively with Si ($R^2 = 0.71$), Al ($R^2 = 0.45$),
764 and K ($R^2 = 0.54$), ~~but~~and negatively with pH ($R^2 = -0.52$; Figs. ~~44e~~12c, S44b,d,f; Table
765 S87).

766

767 **5 Discussion**

768

769 **5.1 Slip rate on the Sparta Fault at Anogia**

770 Average exhumation of the entire scarp up to the present day is 0.7– 0.8 mm yr⁻¹ (Fig. 5a;

771 Table 2).– This compares with an exhumation rate of 1.1–1.2 mm yr⁻¹ up to the 464 B.C.E.

772 earthquake (if an earthquake occurred now, the rate up to the present day would increase).

773 Our data shows an increase in average slip rate during exhumation of the scarp from an initial

774 0.8–0.9 mm yr⁻¹ at between 6.5– and 7.7 kyr ago to 1.0 mm yr⁻¹ from between 3.0 and 6.0 kyr

775 ago up to and 2.5 kyr (Fig. 5e). ~~Average exhumation of the entire scarp up to the present day~~

776 ~~is 0.7– 0.8 mm yr⁻¹ (Fig. 5).~~ These slip rates directly reflect the steeper ³⁶Cl gradient for the

777 lower 4.0 m of the fault scarp compared with the gentler gradient from 4.0 to 6.5 m (Figs. 2

778 and 3c). Although the sampling density is highest over the lowermost 4 m, we have

779 confidence in the lower inferred average slip rate for the higher, older part of the scarp

780 because both our dispersed drill core samples and the Benedetti et al. (2002) profile indicate a

781 lower ³⁶Cl concentration gradient (in trend, rather than absolute values) above 4 m. The MAP

782 model (Fig. 3a) indicates that three scarp exhuming earthquakes may have occurred during
783 5000-6000 years ago (MAP average slip rate 1.1 mm yr⁻¹), which is consistent with an
784 increase in average slip rate during this period observed in the slip rate versus time plot (Fig.
785 5e). The lower rate of exhumation for the upper ~2.5 m reflects an apparent quiescent period
786 prior to these earthquakes. MCMC modelling does not indicate that earthquakes have
787 contributed to exhumation of the Sparta fault more recently than the last historically recorded
788 event at 464 B.C.E. Periods of quiescence appear to characterize normal faults in the
789 Mediterranean region (Cowie et al., 2017; Goodall et al., 2021) and so the recent 2.5 kyr
790 period of quiescence is not necessarily indicative that another earthquake is imminent.
791 This departure from a key conclusion by Benedetti et al. (2002) reflects advances over the past 20
792 years in knowledge of normal fault behaviour.

793
794 Our data do not uniquely specify the number and timing of scarp exhumation events and we
795 have not been able to identify other faults along the eastern flank of the Taygetos
796 Mountains suitable for ³⁶Cl analyses that with the Sparta fault may form part of a system,
797 across which slip is distributed and be suitable for ³⁶Cl analyses, have not been identified
798 along the eastern flank of the Taygetos Mountains. We therefore limit our interpretations to
799 averaged slip rates and the timing of changes in these rates for the Sparta fault at Anogia,
800 rather than attempting to identify individual earthquakes or draw broader
801 influences conclusions on regional fault kinematics and associated seismic hazards.

802 **5.1. Modelling of earthquakes from ³⁶Cl concentration profiles**

803 Our modelling using Schlagenhauf et al. (2010) indicates that five earthquakes provide a best
804 fit to the Sparta fault ³⁶Cl data. The youngest inferred earthquake (2.3 kyr B.P.) corresponds
805 both with the historical 464 B.C.E. event and inflections in the ³⁶Cl data of the 2.0 m long
806 and 3.9 m long profiles. The penultimate inferred earthquake at 2.8 kyr B.P. correlates to an

807 inflection in ^{36}Cl concentration at 2.6 m in our 3.9 m long profile. Because data density
808 decreases above 4.0 m, there are no clear inflections in ^{36}Cl concentrations to base the
809 occurrence of earthquakes on for this segment of the scarp. However, fitting the
810 Schlagenhauf et al. (2010) model to the measured gradient in ^{36}Cl concentrations yields an
811 additional record of three older earthquakes at 3.2 kyr B.P., 3.8 kyr B.P., and 5.9 kyr B.P. to
812 explain the exhumation of the exposed scarp surface. The four most recent earthquakes are
813 clustered within a 1.5 kyr period, whereas nearly 2.5 kyr have elapsed since the last
814 earthquake on the Sparta fault. A lower gradient in ^{36}Cl concentration on the fault scarp
815 above the location of the inferred 3.2 kyr B.P. earthquake also indicates a lower rate of scarp
816 exhumation prior to the 1.5 kyr period of apparently higher earthquake activity. The long
817 recent quiescent interval therefore does not necessarily provide evidence that another (large
818 magnitude) earthquake may be imminent. As a comparison, extensional faults in the central
819 Italian Apennines accumulate meters of displacement over several thousands of years, but
820 also display similar length periods where cumulative slip magnitudes are much lower,
821 because earthquake activity shifts between faults across strike (Cowie et al., 2017). The same
822 may also apply to the Sparta fault and related extensional faults in the region.

823

824 The precision at which we can interpret paleoseismicity is constrained by three factors. These
825 include (i) sparse ^{36}Cl data above 4.0 m on the Sparta fault scarp, (ii) uncertainties in scarp
826 erosion rate, pre-exposure length, and hanging wall surface dip angle and colluvium density
827 (Fig. 4), and (iii) fault scarp impurities that produce noise in the ^{36}Cl data and distortion of
828 potential REY indicators of former soil surfaces. Below, we will explore methodological and
829 geological sources of uncertainty in the ^{36}Cl data, reasons for mineralogical impurities in the
830 Sparta fault scarp, and how the observed REY distribution can be interpreted. This will be
831 achieved by comparing the 2.0 m long profile with the equivalent segment of the 3.9 m long

832 ~~profile because both profiles have been sampled, processed, and analyzed in the same manner~~
833 ~~and at the same time, and therefore provide a measure of repeatability.~~

834

835 **5.2 Methodological and geological sources of uncertainty in the ^{36}Cl data**

836 A feature of the ^{36}Cl data is that our Anogia A and B ^{36}Cl profiles display systematically

837 lower concentrations than the Benedetti et al. (2002) profile (Fig. 2). The Benedetti et al.

838 (2002) profile also displays variations between adjacent sample points that exceed those

839 observed in our profiles. We interpret the systematic differences in ^{36}Cl concentration

840 between our profiles and the Benedetti et al. (2002) profile as reflecting methodological

841 differences related to advances in sample preparation chemistry at PRIME-Lab, Purdue

842 University. For this reason, we elect not to model the Benedetti et al. (2002) data using the

843 MCMC methodology.

844

845 Whereas our Anogia A and B profiles display corresponding trends with increasing elevation

846 on the fault scarp, Anogia B ~~has~~ samples have generally lower ^{36}Cl concentrations (Fig. 2).

847 Indeed, six of its 19 ^{36}Cl concentrations do not overlap within uncertainty with concentrations

848 of corresponding samples on the 3.9 m Anogia A profile, including four points located

849 between 1.0 m and 1.3 m. We interpret these differences as indicating that the fault scarp at

850 Anogia B has been either partly shielded from cosmogenic radiation, has eroded more than

851 the scarp surface at Anogia A, or contains a higher concentration of non-calcite impurities. Of

852 potential additional relevance is that the texture of the scarp surface at Anogia B is smoother

853 than at the location of Anogia A. Because a similarly smooth texture also characterizes the

854 scarp surface presently buried by colluvium mantling the hanging wall, the smooth texture at

855 the location of Anogia B may indicate either recent burial of the scarp surface by colluvium

856 and/or CaCO_3 dissolution/precipitation occurring at a higher rate than at locations where

857 the exposed scarp surface texture is rougher. If a smooth texture reflects erosion through

858 CaCO₃ dissolution, there might be preferential flow, or seepage, of water from the hillslope
859 above the scarp at the location of Anogia B. Observed lumps of colluvium cemented to the
860 Sparta fault scarp, at locations perched above the present hanging wall surface (Fig. S1)
861 partially shield the underlying scarp surface today. However, had this previously occurred at
862 the location of Anogia B, an eroded colluvial lump would be evidenced in the hanging wall
863 sediments. On the contrary, there is no colluvial lump, but rather a sub-horizontal surface is
864 present with an expression that differs little from the surface below the Anogia A profile. The
865 inter-profile differences in ³⁶Cl concentrations illustrate the value in taking samples for ³⁶Cl
866 measurements from more than one vertical profile at a particular location, because ³⁶Cl
867 concentrations can vary either through ~~though~~ spatial variations in non-calcite impurities or
868 past shielding by sediments or bedrock, which can otherwise be difficult to detect. Partial
869 shielding may impact the interpretation of paleoseismicity, including the timing, number and
870 magnitudes of earthquakes, through locally lower ~~inged~~ ³⁶Cl concentrations. A peculiar feature
871 of the ³⁶Cl data is that the profile comprised of small drill core samples generally yields
872 younger exposure ages for the Sparta fault scarp than the 2.0 m and 3.9 m long profiles,
873 which, in turn, are systematically younger than the Benedetti et al. (2002) profile (Fig. 2).
874 The Benedetti et al. (2002) profile displays variations between adjacent sample points that
875 exceed those observed in our profiles and rival variations in ³⁶Cl concentrations that may be
876 attributable to earthquakes. We interpret the systematic differences in ³⁶Cl concentration
877 between the drill core profile, the 2.0 m and 3.9 m profiles, and the Benedetti et al. (2002)
878 profile as reflecting methodological differences related to advances in sample preparation
879 chemistry at PRIME Lab, Purdue University. Similarly, the reason why we can directly infer
880 the 464 B.C.E earthquake at Anogia, in contrast to Benedetti et al. (2002), is attributable to
881 advances in age calculations from ³⁶Cl concentrations.

883
884
885
886
887
888
889
890
891
892
893
894
895
896
897
898
899
900
901
902
903
904
905
906
907

~~Whereas our 2.0 m and 3.9 m long profiles display corresponding trends with increasing elevation on the fault scarp, the 2.0 m profile has generally lower ^{36}Cl concentrations (Fig. 2). Indeed, six of its 19 ^{36}Cl concentrations do not overlap within uncertainty with concentrations of corresponding samples on the 3.9 m profile, including four points located between 1.0 m and 1.3 m. We interpret these differences as indicating that the fault scarp of the 2.0 m profile has been either partly shielded from cosmogenic radiation, has eroded more than the surface of the 3.9 m profile, or contains a higher concentration of impurities. Of potential additional relevance is that the texture of the scarp surface at the location of the 2.0 m profile is smoother than at the location of the 3.9 m profile. Because a similarly smooth texture also characterizes the scarp surface presently buried by colluvium mantling the hanging wall, the smooth texture at the location of the 2.0 m profile may indicate either recent burial of the scarp surface by colluvium and/or CaCO_3 dissolution occurring at a higher rate than at locations where the exposed scarp surface texture is rougher. If a smooth texture reflects erosion through CaCO_3 dissolution, there might be preferential flow, or seepage, of water from the hillslope above the scarp at the location of the 2.0 m profile. Observed lumps of colluvium cemented to the Sparta fault scarp, at locations perched above the present hanging wall surface (Fig. S1) partially shield the underlying scarp surface. However, had this previously occurred at the location of our 2.0 m profile, an eroded colluvial lump would be evidenced in the hanging wall sediments. On the contrary, there is no colluvial lump, but rather a sub-horizontal surface is present with an expression that differs little from the surface below the 3.9 m profile. The inter-profile differences in ^{36}Cl concentrations illustrate the value in taking samples for ^{36}Cl measurements from more than one vertical profile, because evidence of past shielding by sediments or bedrock can otherwise be difficult, at best, to detect. Partial shielding may impact the interpretation of the number of paleoearthquakes and~~

908 ~~result in lower age estimates of earthquakes, with a corresponding decrease in recurrence~~
909 ~~intervals.~~

910

911 **5.3. The effects of mineralogical impurities on ^{36}Cl concentrations profiles**

912 Mineralogical impurities embedded in the fault breccia that comprises the scarp surface
913 appear to be a key geological reason for spatial variations in the concentration of ^{36}Cl .
914 Measurements of chemistry and mineralogy at Anogia B indicate that SiO_2 comprises 0.1–
915 20.8 wt.% of the scarp. Because the concentration of CaCO_3 is inversely correlated with SiO_2
916 (largely quartz), then peaks in SiO_2 might coincide with troughs in ^{36}Cl , although a simple
917 relationship vertically along the scarp is obscured by the relationship between ^{36}Cl
918 concentration and exposure duration. A local peak in SiO_2 of 12–15 wt.% coincides with a
919 local low in ^{36}Cl concentration at Anogia B between about 0.6 and 1.2 m on the scarp (Figs. 2
920 and 7, Tables S1 and S3). A distinct low in ^{36}Cl concentration at 1.6 m also corresponds with
921 a local peak in SiO_2 of 9 wt.%. However, the magnitudes of the variations are inconsistent
922 between these two locations, such that a high peak in SiO_2 corresponds with a small reduction
923 of ^{36}Cl at 0.6–1.2 m and ~~visavice~~ versa at 1.6 m. Because ^{36}Cl is also produced by spallation
924 on K (162 ± 24 atoms $\text{g}^{-1} \text{yr}^{-1}$ at SLHL; Evans et al., 1997), Fe (1.3 ± 0.1 atoms $\text{g}^{-1} \text{yr}^{-1}$ – $1.9 \pm$
925 0.2 atoms $\text{g}^{-1} \text{yr}^{-1}$ at SLHL; Stone, 2005; Moore and Granger, 2019), and Ti (13 ± 3 atoms g^{-1}
926 yr^{-1} at SLHL; Fink et al., 2000), noise in the ^{36}Cl data might also partly reflect the relative
927 abundances of these elements. However, this appears to be insignificant given that measured
928 concentrations of these elements are extremely low (concentrations of K_2O , Fe_2O_3 , and TiO_2
929 are 0–0.12%, 0.03–0.24%, and 0–0.02%, respectively; Fig. S4, Table S3). Other elements,
930 seemingly present as trace amounts of clay, lining pores in the fault breccia (Fig. 7, Table
931 S3), are also an insignificant contributor to variations in ^{36}Cl concentrations. For the Sparta
932 fault at Anogia, quartz embedded in the fault breccia ~~appears to~~ may be the key mineralogical

933 impurity that is likely contributing variance to the ^{36}Cl concentrations, which in turn impacts
934 our ability to obtain unequivocal dates of individual earthquakes. to such an extent that
935 individual earthquakes cannot be reliably identified. Mineralogical impurities embedded in the
936 fault breccia that comprises the scarp surface appear to be a key geological reason for spatial
937 variations in the concentration of ^{36}Cl . This effect is best evidenced when comparing
938 modelled ^{36}Cl concentrations for the 2.0 m long profile (Fig. 3b), including measured
939 mineralogy for each sample location, with modelled ^{36}Cl concentrations for the 3.9 m long
940 and Benedetti et al. (2002) profiles, including mean values of the scarp composition derived
941 from our measured data (Fig. 3a, c, d). Whereas the latter modelled profiles appear smooth,
942 the modelled 2.0 m profile contains inter-sample noise, which reflects variations in calcite
943 abundance, attributable to the additional, and variable, presence of quartz and other minerals,
944 including trace amounts of clay lining pores (Figs. 5–9). Because ^{36}Cl is also produced by
945 spallation on K (162 ± 24 atoms $\text{g}^{-1} \text{yr}^{-1}$ at SLHL; Evans et al., 1997), Fe (1.9 ± 0.2 atoms g^{-1}
946 yr^{-1} at SLHL; Stone, 2005), and Ti (13 ± 3 atoms $\text{g}^{-1} \text{yr}^{-1}$ at SLHL; Fink et al., 2000), noise in
947 the ^{36}Cl data might also partly reflect the relative abundances of these elements. However, for
948 the case of the Sparta fault, this appears to be insignificant given that measured
949 concentrations of these elements are extremely low (concentrations of K_2O , Fe_2O_3 , and TiO_2
950 are 0–0.12%, 0.03–0.24%, and 0–0.02%, respectively; Fig. S3, Table S2).

951
952 Mineralogical impurities may also explain two other enigmatic features in the ^{36}Cl data.
953 Firstly, an apparent age reversal occurs at 3.1 m in the 3.9 m long profile (Fig. 3a). Although
954 this could indicate the location of a former soil horizon and thus inferred displacement by an
955 earthquake, a better model fit is gained by locating an earthquake higher up the scarp at 3.9
956 m. Secondly, ^{36}Cl concentrations at ~4 m in the 3.9 m profile and the Benedetti et al. (2002)
957 data (3.8–4.1 m, Fig. 3a; 3.7–4.3 m, Fig. 3c) are too low to overlap within uncertainty with

958 concentrations modeled using Schlagenhauf et al. (2010). A possible explanation for both
959 enigmatic features is an inability to fully capture the effects of mineralogical impurities on
960 ^{36}Cl production rates. This is largely because, in the absence of mineralogical data for these
961 profiles, we have calculated a mean composition based on the mineralogical data for the 2.0
962 m profile to model ^{36}Cl concentrations. However, even with the mineralogical data, current
963 laboratory techniques for preparing samples for ^{36}Cl measurement may not record
964 mineralogical variations at sufficient precision. In addition to highlighting the importance of
965 mineralogical analyses, we also highlight the value of using a model to identify the likely
966 displacements by paleoearthquakes through fitting model ^{36}Cl concentration profiles to real
967 ones, rather than overtly relying on apparent age reversals. It remains possible that two
968 earthquakes occurred in close succession, but with this data and methodology, we cannot
969 confidently infer both of those.

970

971 **5.4. Estimated magnitude of the 464 B.C.E. earthquake**

972 The 464 B.C.E. earthquake that destroyed Sparta had an estimated moment (M_0) of $1-4$ (\times
973 10^{19}) N m. This is derived from multiplying the vertical displacement of 1.4 m (Fig. 3a-c)
974 with fault dimensions of 20 x 14 km—64 x 14 km, and with a shear modulus of 3.23×10^{10} N
975 m^{-2} (Armijo et al., 1991). The values of 20 km, 14 km, and the shear modulus are from
976 Armijo et al. (1991) and 64 km is the mapped length of the Sparta fault in Figure 1. This
977 estimated range of M_0 values straddles a previous “most probable” estimate of moment by
978 Armijo et al. (1991) of 3×10^{19} N m even though they lacked field constraints on fault slip
979 distance during the Sparta Earthquake. Hence, we conclude from this congruence of the
980 probable value with values based on the vertical displacement modelled from the ^{36}Cl data
981 (Fig. 3), that they are reliable. From the empirically derived equations of Pavlides and Caputo
982 (2004) and a vertical displacement of 1.4 m of the Sparta fault, we calculate a magnitude (M_s)

983 of 6.8–7.2 for the 464 B.C.E. earthquake. Given the severe destruction inflicted upon the
984 Spartan society (REF?), we consider that the upper estimate is most likely. A magnitude 7.2
985 earthquake is also in agreement with the estimate by Armijo et al. (1991), although they
986 based this on ~10 m of vertical displacement. We are less certain of the magnitudes and
987 timing of older earthquakes. However, it appears that the Sparta fault was exhumed by a
988 series of similarly large earthquakes over a period of about 3.5 kyr.

989

990 **5.4. Interpretation of REE-Y distributions and implications for paleoseismicity**

991 REE-Y cannot be used to infer imprints of former soil profiles on the Sparta fault at Anogia.

992 Petrographic analyses indicate that the Sparta fault scarp is composed of a protocataclasite

993 consisting of calcite clasts derived from the host limestone, microcrystalline calcite cement,

994 and quartz (Figs. 6, 7). Furthermore, EDS analysis indicates that trace amounts of clay, such

995 as illite, are lining pores where microcrystalline calcite cement and quartz are located (Fig. 8;

996 Carcaillet et al., 2008). We infer that REE-Y are adsorbed onto clay minerals lining pores in

997 the fine-grained matrix of the fault breccia, as indicated by correlations between REE-Y and

998 each of Al, K, and Si, and Fe ($R^2 = 0.92, 0.87, \text{ and } 0.56, \text{ and } 0.47$, respectively; Fig. S4a-c)

999 and between Y and both Si and Al in the hanging wall colluvium ($R^2 = 0.71 \text{ and } 0.45$,

1000 respectively; Figs. 12c and S4b,c). Supplementary data from the Kaparelli fault ($R^2 = 0.95$ for

1001 Si; Figs. 1a and S5a), and Magnola fault hanging walls ($R^2 = 0.98$ for both Si and Al; Fig.

1002 S5b,c and electronic appendix to Manighetti et al., 2010) also indicate that REE-Y may be

1003 adsorbed to clay embedded in limestone fault scarps. These correlations generally contrast

1004 with a weaker negative correlation between Y and pH ($R^2 = 0.52$) for the hanging wall soil on

1005 the Sparta Fault (Fig. 12c). Soil pH does not appear to be the dominant control on REE-Y

1006 distributions in the Sparta fault scarp, which differs to interpretations on other limestone fault

1007 scarps (Carcaillet et al., 2008; Bello et al., 2023).

1008
1009
1010
1011
1012
1013
1014
1015
1016
1017
1018
1019
1020
1021
1022
1023
1024
1025
1026
1027
1028
1029
1030
1031
1032

We propose a causative relationship between the vertical distributions of REE-Y and clay on the Sparta fault scarp. This reasoning is supported by the following observations:

(i) The Sparta fault scarp REE-Y concentrations are equivalent to (Nuriel et al., 2012; Goodfellow et al., 2017) or higher than those measured elsewhere in platformal limestone (Carcaillet et al., 2008; Mouslopoulou et al., 2011), but Y concentrations are lower than in the adjacent hanging wall soil (REE were not measured in the soil; Tables S6, S8).

(ii) If REE-Y exchange between the soil and fault scarp occurs according to the Carcaillet et al. (2008) model, fractionation of LREE and HREE elements is expected. For example, LREE might be preferentially mobilized (Takahashi et al., 2005; Carcaillet et al., 2008), leading to an enrichment of LREE relative to HREE in the fault scarp, where there are peaks in total REE-Y. Conversely, LREE may be depleted relative to HREE where there are troughs in total REE-Y. However, the proportion of LREE to HREE remains confined to a constant range vertically along the subaerial partsection of Sparta fault scarp (Figs. 10b, 11a), is weakly correlated with total REE-Y ($R^2 = 0.36$; Fig. 11b), and is relatively depleted at all measured depths beneath the soil surface (Fig. 10b).

(iii) There is no systematic decrease with distance above the hanging wall in total REE-Y along the vertical scarp profile (Fig. 10a, b), in contrast to declining concentrations with distance above the hanging wall on the Magnola fault (Carcaillet et al., 2008).

Adsorption of REE-Y onto clay has been observed in regolith (Borst et al., 2020) but has not been previously discussed in the context of interpreting paleoseismicity on limestone fault scarps.

1033
1034
1035
1036
1037
1038
1039
1040
1041
1042
1043
1044
1045
1046
1047
1048
1049
1050
1051
1052
1053
1054
1055
1056
1057

Although we infer that adsorption of REE-Y onto clay minerals embedded in fault breccia dominates on the Sparta fault, the approximate coincidence of the subsurface peak in scarp LREE/HREE and total REE-Y with the mid-profile peak in soil pH (Figs. 10, 12a, b) provides evidence of REE-Y exchange between the scarp and the soil. However, the consequence is LREE depletion in the scarp, rather than enrichment (Fig. 10b), and it is unclear why this apparent depletion is not replicated on the subaerially exposed scarp. One possibility is that colluvium accumulation postdates the most recent earthquake although, if so, low ³⁶Cl concentrations in the buried scarp surface indicate that the soil accumulation was co-seismic with the last earthquake or accumulated soon afterwards. It is also unclear why colluvium would accumulate only after the most recent earthquake. An alternative possibility is that a superficial LREE-depleted zone has been eroded from the subaerial scarp surface through dissolution. This would imply erosion of centimeters of scarp surface since the last known earthquake on the Sparta fault at 464 B.C.E. (~~assuming with an~~ erosion rate of 0.01 mm yr⁻¹ over the past 2500 years, ~~there would remove~~ ~~be implies~~ 2.5 cm of scarp surface ~~over the past 2.5 kyr~~). Yet another possibility is that perhaps more time is required to increase LREE to concentrations seen on the subaerial scarp surface, but 2500 years have already passed since the most recent known earthquake and maximum REE-Y enrichment has been inferred to occur within 500 years on the Spilli and Magnola faults (Manighetti et al., 2010; Mouslopoulou et al., 2011). Alternatively, LREE enrichment ~~may continue~~ occurs after scarp exhumation, perhaps through exchange with aeolian dust fallout, as has been observed in Dead Sea halite (Censi et al., 2023). Such dust inputs may supply REE-Y (Yang et al., 2007), as indicated by the correlation between Y and Si in the hanging wall colluvium (Fig. 12b, c), contribute fine-grained mineral soil to the hanging wall colluvium, and may lower soil pH through buffering locally-sourced CaCO₃. However, given that inputs of Saharan dust are

1058 ubiquitous throughout the Mediterranean (Stuut et al., 2009) and can comprise a large
1059 component of soils in the region (Muhs et al., 2010; Styllas et al., 2023), similar patterns of
1060 LREE depletion in the soil-covered scarp surface relative to the subaerial scarp surface are
1061 expected to have been observed elsewhere, which is not the case (Carcaillet et al., 2008;
1062 Manighetti et al., 2010; Mouslopoulou et al., 2011; Tesson et al., 2016; Bello et al., 2023).
1063
1064 For the Sparta fault scarp, the presence of clay likely relates to fault breccia formation at
1065 considerable depths beneath the Earth's surface, rather than subaerial weathering processes.
1066 The formation of protocataclasite occurs beneath the Earth's surface at depths that may range
1067 from meters to up to thousands of meters. A model for this involves fluids moving along the
1068 Sparta fault, primarily associated with seismic events. These fluids dissolve CaCO₃ from the
1069 host-limestones and potentially also silicate minerals from psammitic and pelitic
1070 (meta)sediments, where they are dissected by the fault. In association with variations in
1071 temperature and pressure along the fault, chemical saturation of these fluids results in
1072 precipitation of clay, quartz, and microcrystalline calcite, which cements clasts of host-rock
1073 derived limestone into the fault breccia. Subsequent faulting re-fractures the breccia and
1074 particle comminution over time produces quartz grains that are rounded-to-angular in shape,
1075 randomly oriented, and <50 μm (Figs. 6, 8). The fault breccia may also have undergone
1076 multiple generations of microcrystalline calcite re-cementing from re-circulating fluids. As an
1077 alternative to a dissolution-precipitation model, clay and quartz emplacement may involve
1078 fluid entrainment of particles and grains from clay- and quartz-bearing sedimentary units
1079 during faulting, as has been observed elsewhere (e.g., Darwin, 1840; Roy, 1946; Brandon,
1080 1972; Röshoff and Cosgrove, 2002). This process may also be accompanied by comminution
1081 of fault-zone quartz grains derived from psammitic rocks. We tentatively exclude a
1082 contemporary aeolian source for the clay and quartz because there is no documented

1083 mechanism to transport clay particles and quartz grains from the soil to centimeters into a
1084 fault scarp. We cannot distinguish soil to scarp clay and quartz migrations on the Sparta fault
1085 which has been observed, for example, at the micrometer scale in surface coatings on the
1086 Magnola fault, because that scarp is comprised of pure carbonate (Carcaillet et al., 2008). It is
1087 likely that limestone fault scarps are generally composed of fault breccias (Agosta and Aydin,
1088 2006; Carcaillet et al., 2008; Nuriel et al., 2012) and that where a fault intersects varying
1089 lithologies, chemical and mineralogical heterogeneities may occur in the fault breccia, as
1090 observed on the Sparta fault. Where they occur, these heterogeneities may control the spatial
1091 distribution of REE-Y, independent of any spatial reorganization of REE-Y attributable to
1092 subaerial weathering. If, as we infer, the spatial patterning of REE-Y, quartz, and clay is
1093 inherited from depth, the observed wave-like signal (Figs. 7, 10) may reflect sorting and
1094 cementing of breccia around surface asperities on the fault plane. The resulting infilling of
1095 depressions with fault gouge may create a successively more polished and localized fault
1096 plane along which friction is lowered, thereby permitting larger slip (i.e., larger earthquakes)
1097 along the fault (Sagy and Brodsky, 2009). Whereas REE-Y concentrations do not appear to
1098 be a reliable indicator of Holocene paleoseismicity ~~alongof~~ the Sparta fault, they may instead
1099 reveal processes that localize slip to a discrete fault plane.

1100
1101 Whereas the Sparta Fault displays concentrations of clay and quartz impurities that are much
1102 higher than on other reported limestone fault scarps, ~~there are three~~ general implications
1103 emerge for using REE-Y in making inferences of paleoseismicity. Firstly, the potential
1104 control on REE-Y distributions of even trace amounts of non-calcite impurities in the breccia
1105 comprising fault scarps should be considered through analyses of thin sections in addition to
1106 scarp chemistry. Secondly, soil acidity and REE-Y enrichment, including any resulting
1107 exchange with the buried scarp, may peak some tens of centimeters below the colluvium

1108 surface. Peaks in REE-Y concentrations on subaerial fault scarp surfaces may not therefore
1109 reflect former soil surfaces, even if there is soil-scarp exchange of REE-Y. In addition, the
1110 Sparta fault scarp REE-Y data indicate that it may be rewarding to focus on up-scarp
1111 variations in LREE/HREE ratios rather than on REE-Y concentrations, because these may be
1112 a sensitive indicator of REE-Y exchange processes occurring beneath soil covers (Fig 10b).
1113 Thirdly/Lastly, relationships between REE-Y distributions and soil mineralogy should be
1114 more closely assessed, in addition to the commonly modelled and studied effects of pH (e.g.,
1115 Carcaillet et al., 2008; Manighetti et al., 2010; Mouslopoulou et al., 2011; Moraetis et al.,
1116 2015, 2023; Tesson et al., 2016; Bello et al., 2023). Fine grained mineral inputs through
1117 aeolian dust fallout comprise substantial volumes of Mediterranean soils (Muhs et al., 2010;
1118 Styllas et al., 2023) and decadal to millennial ~~temporal~~ variations in dust fluxes may directly
1119 impact on REE-Y distributions in hanging wall soils and potentially in scarp surfaces, in
1120 locations where soil-scarp REE-Y exchange is important. These fluctuations may contribute
1121 to REE-Y patterns in soils that are difficult to predict and in scarp surfaces reflect (climatic
1122 and pedogenic) processes that may complicate potential paleoseismic inferences.
1123
1124 Moraetis et al. (2023) consider REE-Y analyses an established method in paleoseismicity.
1125 Our detailed study errs towards caution; there remain important uncertainties regarding
1126 processes of REE-Y enrichment and depletion in limestone fault scarps. Indeed, we maintain
1127 that there is considerable uncertainty regarding how the resulting patterns should be
1128 interpreted with respect to paleoseismicity. ~~Fundamentally~~Fundamentally, it ~~It is also~~
1129 ~~presently~~remains unclear how far into buried scarp surfaces the REE-Y can be adsorbed from
1130 soil or incorporated into calcite through dissolution-precipitation. A dissolution rate of 0.001
1131 mm/year yr⁻¹ will erode 1 cm from a subaerially exposed scarp surface over 10 000 years,
1132 which is about the timescale considered to be relevant to assessing full seismic cycles and

1133 therefore making accurate assessments of paleoseismicity (Mouslopoulou et al., 2012; Tesson
1134 et al., 2016). Even such a slow rate of subaerial scarp dissolution will therefore remove any
1135 REE-Y signals inherited from former soil cover unless that exchange extends to centimeters
1136 into the scarp.

1137 Moraetis et al. (2023) state that REE-Y analyses are an established method in
1138 paleoseismicity. We agree that there do, however, remain important uncertainties regarding
1139 processes of REE-Y enrichment and depletion in limestone fault scarps but add that there is
1140 also considerable uncertainty regarding how the resulting patterns should be interpreted with
1141 respect to paleoseismicity. REY cannot be used to infer imprints of former soil profiles on the
1142 Sparta fault at Anogia. Petrographic analyses indicate that the Sparta fault scarp is composed
1143 of a protocataclasite consisting of calcite clasts derived from the host limestone,
1144 microcrystalline calcite cement, and quartz (Figs. 5, 6). Furthermore, EDS analysis indicates
1145 that trace amounts of clay, such as illite, are lining pores where microcrystalline calcite
1146 cement and quartz are located (Fig. 7; Carcaillet et al., 2008). Given the correlations between
1147 REY and each of Al, K, and Si ($R^2 = 0.92, 0.87, \text{ and } 0.56$, respectively; Fig. S2a-c), we infer
1148 that the clays embedded in the fault scarp are hosting REY. This is a likely explanation for
1149 why REY peaks 0.4 m below the current soil surface (Fig. 9), rather than at the soil surface as
1150 has been observed on the Magnola fault in Italy (Manighetti et al., 2010).

1151

1152

1153 The formation of protocataclasite occurs beneath the Earth's surface at depths that may range
1154 from meters to up to thousands of meters. A model for this involves fluids moving along the
1155 Sparta fault, primarily associated with seismic events. These fluids dissolve CaCO_3 from the
1156 host limestones and potentially also silicate minerals from psammitic and pelitic
1157 (meta)sediments, where they are dissected by the fault. In association with variations in

1158 temperature and pressure along the fault, chemical saturation of these fluids results in
1159 precipitation of clay, quartz, and microcrystalline calcite, which cements clasts of host rock
1160 derived limestone into the fault breccia. Subsequent faulting re fractures the breccia and
1161 particle comminution over time produces quartz grains that are rounded to angular in shape,
1162 randomly oriented, and $<50\ \mu\text{m}$ (Figs. 5, 7). The fault breccia may also have undergone
1163 multiple generations of microcrystalline calcite re cementing from re circulating fluids. As an
1164 alternative to a dissolution precipitation model, clay and quartz emplacement may involve
1165 fluid entrainment of particles and grains from clay and quartz bearing sedimentary units
1166 during faulting, as has been observed elsewhere (e.g., Darwin, 1840; Roy, 1946; Brandon,
1167 1972; Röshoff and Cosgrove, 2002). This process may also be accompanied by comminution
1168 of fault zone quartz grains derived from psammitic rocks. We tentatively exclude a
1169 contemporary aeolian source for the clay and quartz because there is no documented
1170 mechanism to transport clay particles and quartz grains from the soil to centimeters into a
1171 fault scarp. We cannot distinguish soil to scarp clay and quartz migrations on the Sparta fault
1172 which has been observed, for example, at the micrometer scale in surface coatings on the
1173 Magnola fault, because that scarp is comprised of pure carbonate (Carcaillet et al., 2008). It is
1174 likely that limestone fault scarps are generally composed of fault breccias (Agosta and Aydin,
1175 2006; Carcaillet et al., 2008; Nuriel et al., 2012) and that where a fault intersects varying
1176 lithologies, chemical and mineralogical heterogeneities may occur in the fault breccia, as
1177 observed on the Sparta fault. Where they occur, these heterogeneities may control the spatial
1178 distribution of REY, independent of any spatial reorganization of REY attributable to
1179 subaerial weathering.

1180

1181 REY correlates with inferred clay abundances on the Sparta fault scarp (Fig. 9), rather than
1182 systematically with former soil profiles inferred from ^{36}Cl concentrations. A correlation of

1183 REY with Si and Al is indeed observed in the soils mantling the Sparta ($R^2 = 0.71$ and 0.45 ,
1184 respectively; Figs. 11c and S2b,c), Kaparelli ($R^2 = 0.95$ for Si; Figs. 1a and S4a), and
1185 Magnola fault hanging walls ($R^2 = 0.98$ for both Si and Al; Fig. S4b,c and electronic
1186 appendix to Manighetti et al., 2010). These correlations generally contrast with a weaker
1187 negative correlation between Y and pH ($R^2 = 0.52$) for the hanging wall soil on the Sparta
1188 Fault (Fig. 11c). We propose a causative relationship between the vertical distributions of
1189 REY and clay on the Sparta fault scarp. The presence of clay likely relates to fault breccia
1190 formation at considerable depths beneath the Earth's surface, rather than subaerial weathering
1191 processes. This reasoning is supported by the following observations:

- 1192 (i) — The Sparta fault scarp REY concentrations are equivalent to (Nuriel et al., 2012;
1193 Goodfellow et al., 2017) or higher than those measured elsewhere in platform
1194 limestone (Carcaillet et al., 2008; Mouslopoulou et al., 2011), but yttrium
1195 concentrations are lower than in the adjacent hanging wall soil (rare earth elements
1196 were not measured; Tables S5, S7).
- 1197 (ii) — If REY exchange between the soil and fault scarp occurs according to the Carcaillet
1198 et al. (2008) model, fractionation of LREY and HREY elements is expected. For
1199 example, LREY might be preferentially mobilized (Takahashi et al., 2005;
1200 Carcaillet et al., 2008), leading to an enrichment of LREY relative to HREY in the
1201 fault scarp, where there are peaks in total REY. Conversely, LREY may be depleted
1202 relative to HREY where there are troughs in total REY. However, the proportion of
1203 LREY to HREY remains constant vertically along the Sparta fault scarp (Fig. 10).
- 1204 (iii) — There is no systematic decrease in total REY along the vertical scarp profile (Fig.
1205 9), in contrast to declining concentrations with distance above the hanging wall on
1206 the Magnola fault (Carcaillet et al., 2008).

1207 Whereas these observations discount subaerial weathering as the dominant mechanism for
1208 REY enrichment and depletion on the Sparta fault, there may be some weathering induced
1209 exchange. This is evidenced by the peak in REY on the buried Sparta fault scarp correlating
1210 with the peak in soil acidity (Figs. 9, 11a, b), but which notably occurs in the subsurface,
1211 rather than at the soil surface. If, as we infer, the spatial patterning of REY, quartz, and clay
1212 (as indicated by Al) is inherited from depth, the observed wave-like signal (Figs. 6, 9) may
1213 reflect sorting and cementing of breccia around surface asperities on the fault plane. The
1214 resulting infilling of depressions with fault gouge may create a successively more polished
1215 and localized fault plane along which friction is lowered, thereby permitting larger slip (i.e.,
1216 larger earthquakes) along the fault (Sagy and Brodsky, 2009). Whereas REY concentrations
1217 do not appear to be a reliable indicator of Holocene paleoseismicity along the Sparta fault,
1218 they may instead reveal processes that localize slip to a discrete fault plane.

1219

1220 **6 Conclusion**

1221

1222 Modelling of ^{36}Cl data from the Sparta fault at Anogia, Greece, indicates an increase in
1223 average slip rate during exhumation of the scarp from 0.8–0.9 mm yr⁻¹ at between 6.5–7.7 and
1224 6.5 kyr ago to 1.0 mm yr⁻¹ from between 6.5 6.5 kyr ago up to and 2.5 kyr ago (the timing if
1225 the historic 464 B.C.E. earthquake (Fig. 5). Average exhumation of the entire scarp up to the
1226 present day is 0.7–0.8 mm yr⁻¹. Modelling does not indicate that earthquakes may have
1227 contributed to exhumation of the Sparta fault more recently than the last historically recorded
1228 event at since 464 B.C.E. Recent quiescence, with a duration of 2.5 kyr, may be indicating
1229 cyclic behavior, where clusters of earthquakes are separated by periods of quiescence that
1230 may extend over thousands over years, as has been reported on other normal faults in the
1231 Mediterranean region. The recent 2.5 kyr long period of quiescence may not be indicative

1232 that another earthquake is imminent but may rather be a part of cyclic behavior, where
1233 clusters of earthquakes are separated by periods of quiescence that may extend over
1234 thousands over years, as occurs on other normal faults in the Mediterranean region.

1235
1236 ~~In applying cosmogenic ^{36}Cl exposure age dating and rare earth elements and yttrium (REY)~~
1237 ~~measurements to unravelling the paleoseismic history of the Sparta fault, Greece, we~~
1238 ~~conclude the following: Modeling of ^{36}Cl concentrations along two vertical profiles on the~~
1239 ~~Sparta Fault, closely adjacent to a ^{36}Cl concentration profile previously measured and~~
1240 ~~interpreted by Benedetti et al. (2002), indicates that the scarp was likely exhumed over 5~~
1241 ~~earthquakes, including one at $\sim 2.3 \pm 0.2$ kyr B.P., which correlates with the 464 B.C.E. event.~~
1242 ~~Four earthquakes were clustered within a 1.5 kyr period that culminated with the 464 B.C.E.~~
1243 ~~event. Cumulative uplift was as high as 2.8 mm yr^{-1} during that period, compared with ~ 0.6~~
1244 ~~0.9 mm a^{-1} over the preceding 2.7–4.4 kyr. Because earthquake activity may shift between~~
1245 ~~faults in extensional settings, a large magnitude earthquake is not necessarily indicated as~~
1246 ~~being overdue by the ~ 2.5 kyr that have elapsed since the 464 B.C.E. event. More generally,~~
1247 ~~accurate identification of individual earthquakes is presently constrained by spatial variations~~
1248 ~~in ^{36}Cl concentration profiles that reflect neither exposure duration nor imprints of former soil~~
1249 ~~profiles. In cases where this is attributable to mineralogical variations, such as in the Sparta~~
1250 ~~fault scarp, present chemical preparation techniques for AMS measurement of ^{36}Cl may~~
1251 ~~insufficiently account for those variations.~~

1252
1253 The Sparta fault scarp is impure; it is composed of fault breccia, which contains quartz and
1254 clay-lined pores in addition to calcite. The vertical distribution of REYREE-Y is highly
1255 correlated with the pore-clay and may indicate processes that localize slip to a discrete fault
1256 plane of fault evolution deep below the ground surface. The potential exchange of REYREE-

1257 Y between the hanging wall colluvium and the adjacent footwall scarp is overwhelmed at this
1258 site by REYREE-Y attached to the pore clays inherited from depth. Because of this,
1259 Holocene earthquakes and their slip distances and magnitudes cannot be inferred for the
1260 Sparta fault from REYREE-Y concentrations. Whereas tThis is probably true also for similar
1261 impure limestone fault scarps elsewhere, other controls on REE-Y distributions, in addition to
1262 hanging wall soil pH, should be evaluated in attempting paleoseismic inferences more
1263 generally from normal fault scarps developed in limestone.-
1264

1265 **Author contribution**

1266 AS and APS conceived the study and acquired the funding for RF, BWG, APS, and AS
1267 supervised RF, APS, AS, APS, BWG, MWC, and RF, and BWG participated in fieldwork.
1268 RF conducted the analysis of scarp composition, and made initial interpretations, and
1269 compiled an initial manuscript as a part of research studies at Stockholm University. BWG
1270 made performed additional analyses, and including earthquake modelling, and led
1271 writingwrote the manuscript of this manuscript. GC led the laboratory preparation of samples
1272 for ³⁶Cl measurement, in which together with BWG also participated. GC, and calculated ³⁶Cl
1273 concentrations from the AMS data. All authors contributed to data interpretation and
1274 manuscript editing.

1275 **Competing interests**

1276 Arjen P. Stroeven is a member of the editorial board for Solid Earth.

1277 **Acknowledgements**

1278 We thank Mikael Amlert for his assistance with field safety and sampling, Giorgos Maneas,
1279 station manager of the Navarino Environmental Observatory (NEO), for his extensive
1280 assistance with field logistics, and our deceased friend, Dan Zetterberg, Department of
1281 Geological Sciences, Stockholm University, for his assistance with thin section preparations.
1282 This project was funded by the Stockholm University Research School for teachers focusing
1283 on Natural Hazards financed by the Swedish Research Council and by a grant from NEO. We
1284 gratefully acknowledge funding for fieldwork from the Swedish Society for Anthropology
1285 and Geography Andréé Fund to Fritzon.

1286 **References**

- 1287 Agosta, F. and Aydin, A.: Architecture and deformation mechanism of a basin bounding
1288 normal fault in Mesozoic platform carbonates, central Italy. Journal of Structural
1289 Geology, 28, 1445–1467, 2006.
- 1290 Armijo, R., Lyon-Caen, H., and Papanastassiou, D.: A possible normal-fault rupture for the
1291 464 BC Sparta earthquake. Nature, 351, 137–139, doi:10.1038/351137a0, 1991.
- 1292 Bello, S., Perna, M.G., Consalvo, A., Brozzetti, F., Galli, P., Cirillo, D., Andrenacci, C.,
1293 Tangari, A.C., Carducci, A., Menichetti, M., Lavecchia, G., Stoppa, F., and Rosatelli, G.:
1294 Coupling rare earth element analyses and high-resolution topography along fault scarps to

1298 [investigate past earthquakes: A case study from the Southern Apennines \(Italy\).](#)
1299 [Geosphere, X19, 1348–241371, <https://doi.org/10.1130/GES02627.1>, 2023.](#)

1300 Benedetti, L., Finkel, R., Papanastassiou, D., King, G., Armijo, R., Ryerson, F., Farber, D.,
1301 and Flerit, F.: Post-glacial slip history of the Sparta fault (Greece) determined by ^{36}Cl
1302 cosmogenic dating: Evidence for non-periodic earthquakes. *Geophysical Research*
1303 *Letters*, 29, 1246–, [doi: 10.1029/2001GL014510](https://doi.org/10.1029/2001GL014510), 2002.

1304 [Benedetti, L., Manighetti, I., Gaudemer, Y., Finkel, R., Malavieille, J., Pou, K., Arnold, M.,](#)
1305 [Aumaître, G., Bourlès, D., and Keddadouche, K.: Earthquake synchrony and clustering on](#)
1306 [Fucino faults \(Central Italy\) as revealed from in situ \$^{36}\text{Cl}\$ exposure dating. *Journal of*](#)
1307 [Geophysical Research, Solid Earth, 118, 4948–4974, 2013.](#)

1308 [Borst, A. M., Smith, M. P., Finch, A. A., Estrade, G., Villanova-de-Benavent, C., Nason, P.,](#)
1309 [Marquis, E., Horsburgh, N. J., Goodenough, K. M., Xu, C., Kynický, J. and Geraki,](#)
1310 [K.: Adsorption of rare earth elements in regolith-hosted clay deposits. *Nature*](#)
1311 [Communications, 11, 4386, 2020.](#)

1312 Brandon, A: Clastic dykes in the Namurian shales of County Leitrim, Republic of Ireland.
1313 *Geological Magazine*, 109, 361–367, 1972.

1314 [Bubeck, A., Wilkinson, M., Roberts, G. P., Cowie, P. A., McCaffrey, K. J. W., Phillips, R.,](#)
1315 [and Sammonds, P.: The tectonic geomorphology of bedrock scarps on active normal](#)
1316 [faults in the Italian Apennines mapped using combined ground penetrating radar and](#)
1317 [terrestrial laser scanning. *Geomorphology*, 237, 38–51, 2015.](#)

1318 Carcaillet, J., Manighetti, I., Chauvel, C., Schlagenhauf, A., and Nicole, J.-M.: Identifying
1319 past earthquakes on an active normal fault (Magnola, Italy) from the chemical analysis of
1320 its exhumed carbonate fault plane. *Earth and Planetary Science Letters*, 271, 145–158,
1321 [doi: 10.1016/j.epsl.2008.03.059](https://doi.org/10.1016/j.epsl.2008.03.059), 2008.

1322 [Censi, P., Sirota, I., Zuddas, P., Lensky, N.G., Crouvi, O., Cangemi, M., and Piazzese, D.:](#)
1323 [Rare earths release from dissolving atmospheric dust and their accumulation into](#)
1324 [crystallising ~~crystallizing~~ halite: The Dead Sea example. *Science of the Total*](#)
1325 [Environment, 875, 162682, 2023.](#)

1326 Cowie, P.A., Phillips, R.J., Roberts, G.P., McCaffrey, R.E.E., K., Zijerveld, L.J.J.,
1327 Gregory, L.C., Faure Walker, J., Wedmore, L.N.J., Dunai, T.J., Binnie, S.A., Freeman,
1328 S.P.T.H., Wilcken, K., Shanks, R.P., Huisman, R.S., Papanikolaou, I., Michetti, A.M.,
1329 and Wilkinson, M.: Orogen-scale uplift in the central Italian Apennines drives episodic
1330 behaviour of earthquake faults. *Scientific Reports*, 7, 44858, 2017.

1331 Darwin, C: Geological observations in the volcanic islands and parts of South America
1332 visited during the voyage of H.M.S. Beagle. London, 1840.

1333 [Dawood, R., Matmon, A., Benedetti, L., ASTER Team, and Siman-Tov, S.: Multi-segment](#)
1334 [earthquake clustering as inferred from \$^{36}\text{Cl}\$ exposure dating, the Bet Kerem fault system,](#)
1335 [northern Israel. *Tectonics*, 43, e2023TC007953, 2024.](#)

1336 Dramis, F, and Blumetti, A.M.: Some considerations concerning seismic geomorphology and
1337 paleoseismology. *Tectonophysics*, 408, 177–191, 2005.

1338 Evans, J.M, Stone, J.O.H., Fifield, L.K., and Cresswell, R.G.: Cosmogenic chlorine-36
1339 production in K-feldspar. *Nuclear Instruments and Methods in Physics Research B*, 123,
1340 334–340, 1997.

1341 Fink, D., Vogt, S., and Hotchkis, M.: Cross-sections for ^{36}Cl from Ti at $E_p = 35\text{--}150\text{ MeV}$:
1342 Applications to in-situ exposure dating. *Nuclear Instruments and Methods in Physics*
1343 *Research B*, 172, 861–866, 2000.

1344 [Friedrich, A. M., Wernicke, B. P., Niemi, N. A., Bennett, R.A., and Davis, J.L.: Comparison](#)
1345 [of geodetic and geologic data from the Wasatch region, Utah, and implications for the](#)
1346 [spectral character of Earth deformation at periods of 10 to 10 million years, *Journal of*](#)
1347 [Geophysical Research: Solid Earth, 108, 2199, 2003.](#)

- 1348 Godey, S., Bossu, R., and Guilbert, J.: Improving the Mediterranean seismicity picture thanks
1349 to international collaborations. *Physics and Chemistry of the Earth, Parts A/B/C*, 63, 3–
1350 11, [doi:10.1016/j.pce.2013.04.012](https://doi.org/10.1016/j.pce.2013.04.012), 2013.
- 1351 [Goodall, H. J., Gregory, L. C., Wedmore, L. N. J., McCaffrey, K. J. W., Amey, R. M.](#)
1352 [J., Roberts, G. P., Shanks, R.P., Phillips, R.J., and Hooper, A. Determining histories of](#)
1353 [slip on normal faults with bedrock scarps using cosmogenic nuclide exposure data.](#)
1354 [Tectonics, 40, e2020TC006457, 2021.](#)
- 1355 Goodfellow, B.W., Viola, G., Bingen, B., Nuriel, P., and Kylander-Clark, A.: Paleocene
1356 faulting in SE Sweden from U-Pb dating of slickenfiber calcite. *Terra Nova*, 29, 321–328.
1357 <https://doi.org/10.1111/ter.12280>, 2017.
- 1358 Gürpınar, A.: The importance of paleoseismology in seismic hazard studies for critical
1359 facilities. *Tectonophysics*, 408, 23–28, [doi: 10.1016/j.tecto.2005.05.042](https://doi.org/10.1016/j.tecto.2005.05.042), 2005.
- 1360 [Hastings, W.K.: Monte Carlo sampling methods using Markov chains and their applications.](#)
1361 [Biometrika, 57, 97–109, 1970.](#)
- 1362 Hickson, C.J. and Juras, S.J.: Sample contamination by grinding. *Canadian Mineralogist*, 24,
1363 585–589, 1986.
- 1364 Hutchison, C.S.: *Laboratory Handbook of Petrographic Techniques*. Wiley-Interscience, New
1365 York, 527 pp, 1974.
- 1366 [Iezzi, F., Roberts, G., Faure Walker, J., Papanikolaou, I., Ganas, A., Deligiannakis, G., Beck,](#)
1367 [J., Wolfers, S. and Gheorghiu, D.: Temporal and spatial earthquake clustering revealed](#)
1368 [through comparison of millennial strain-rates from ³⁶Cl cosmogenic exposure dating and](#)
1369 [decadal GPS strain-rate. Scientific Reports, 11, 23320, 2021](#)[https://doi.org/10.1038](https://doi.org/10.1038/s41598-021-02131-3)
1370 [/s41598-021-02131-3.](https://doi.org/10.1038/s41598-021-02131-3)
- 1371 Institute for Geology and Subsurface Research: Sparti Sheet, photogeological map of Greece,
1372 1969.
- 1373 Jolivet, L., Faccenna, C., Huet, B., Labrousse, L., Le Pourhiet, L., Lacombe, O., Lecomte, E.,
1374 Burov, E., Denèle, Y., Brun, J.-P., Philippon, M., Paul, A., Salaün, G., Karabulut, H.,
1375 Piromallo, C., Monié, P., Gueydan, F., Okay, A.I., Oberhänsli, R., Pourteau, A., Augier,
1376 R., Gadenne, L., and Driussi, O.: Aegean tectonics: Strain localisation, slab tearing and
1377 trench retreat. *Tectonophysics*, 597–598, 1–33, 2013.
- 1378 Lifton, N.A., Bieber, J.W., Clem, J.M., Duldig, M.L., Evenson, P., Humble, J.E., and Pyle,
1379 R.: Addressing solar modulation and long-term uncertainties in scaling secondary cosmic
1380 rays for in situ cosmogenic nuclide applications. *Earth and Planetary Science Letters*,
1381 239, 140–161, 2005.
- 1382 Lifton, N.A., Sato, T. and Dunai, T.J.: Scaling in situ cosmogenic nuclide production rates
1383 using analytical approximations to atmospheric cosmic-ray fluxes. *Earth and Planetary*
1384 *Science Letters*, 386, 149–160, 2014.
- 1385 Lifton, N.A., Smart, D.F. and Shea, M.A.: Scaling time-integrated in situ cosmogenic
1386 nuclide production rates using a continuous geomagnetic model. *Earth and Planetary*
1387 *Science Letters*, 268, 190–201, 2008.
- 1388 Manighetti, I., Boucher, E., Chauvel, C., Schlagenhauf, A. and Benedetti, L.: Rare earth
1389 elements record past earthquakes on exhumed limestone fault planes. *Terra Nova*, 22,
1390 477–482, [doi: 10.1111/j.1365-3121.2010.00969.x](https://doi.org/10.1111/j.1365-3121.2010.00969.x), 2010.
- 1391 Marrero, S.M., Phillips, F.M., Caffee, M.W. and Gosse, J.C.: CRONUS-Earth cosmogenic
1392 ³⁶Cl calibration. *Quaternary Geochronology*, 31, 199–219, 2016.
- 1393 McCalpin, J.P.: *Paleoseismology*, Academic press, 613 pp., 2009.
- 1394 McDonough, W.F. and Sun, S.-s.: The composition of the Earth. *Chemical Geology*, 120,
1395 223–253, 1995.
- 1396 [Metropolis, N., Rosenbluth, A. W., Rosenbluth, M. N., Teller, A. H. and Teller, E.: Equation of state](#)
1397 [calculations by fast computing machines. Journal of Chemical Physics, 21, 1087–1092, 1953.](#)

- 1398 Michetti, A.M., Audemard ~~M.~~, F.A. and Marco, S.: Future trends in paleoseismology:
1399 Integrated study of the seismic landscape as a vital tool in seismic hazard analyses
1400 Tectonophysics, 408, 3–21, 2005.
- 1401 Mitchell, S.G., Matmon, A., Bierman, P.R., Enzel, Y., Caffee, M., and Rizzo, D.:
1402 Displacement history of a limestone normal fault scarp, northern Israel, from cosmogenic
1403 ³⁶Cl/Cl-36. Journal of Geophysical Research-: Solid Earth, 106, 4247–4264, doi:
1404 [10.1029/2000JB900373](https://doi.org/10.1029/2000JB900373), 2001.
- 1405 [Moore, A. K. and Granger, D. E.: Calibration of the production rate of cosmogenic ³⁶Cl from
1406 Fe. Quaternary Geochronology, 51, 87–98, 2019.](#)
- 1407 ~~Moraetis, D., Mouslopoulou, V., and Pratikakis, A.: Sorption of the Rare Earth Elements and
1408 Yttrium (REE-Y) in calcite: the mechanism of a new effective tool in identifying
1409 paleoearthquakes on carbonate faults. Abstract. Geophysical Research Abstracts, 17,
1410 EGU2015-3437, 2015.~~
- 1411 [Moraetis, D., Mouslopoulou, V., Pratikakis, A., Begg J., and Pracejus, B.: The mechanism of
1412 REE-Y impregnation on active carbonate normal fault scarps. Applied Geochemistry,
1413 155, 105703, 2023.](#)
- 1414 Mouslopoulou, V., Moraetis, D., and Fassoulas, C.: Identifying past earthquakes on carbonate
1415 faults: Advances and limitations of the ‘Rare Earth Element’ method based on analysis of
1416 the Spili Fault, Crete, Greece. Earth and Planetary Science Letters, 309, 45–55, 2011.
- 1417 [Mouslopoulou, V., Nicol, A., Walsh, J.J., Begg, J.G., Townsend, D.B., and Hristopulos,
1418 D.T.: Fault-slip accumulation in an active rift over thousands to millions of years and the
1419 importance of paleoearthquake sampling, Journal of Structural Geology, 36, 71–80, 2012.](#)
- 1420 Mozafari, N., Özkaymak, C., Sümer, Ö, Tikhomirov, D., Uzel, B., Yeşilyurt, S., Ivy-Ochs, S.,
1421 Vockenhuber, C., Sözbilir, H., and Akçar, N.: Seismic history of western Anatolia during
1422 the last 16 kyr determined by cosmogenic ³⁶Cl dating. Swiss Journal of Geosciences, 115,
1423 5, <https://doi.org/10.1186/s00015-022-00408-x>, 2022.
- 1424 Muhs, D.R., Budahn, J., Avila, A., Skipp, G., Freeman, J. and Patterson, D.: The role of
1425 African dust in the formation of Quaternary soils on Mallorca, Spain and implications for
1426 the genesis of Red Mediterranean soils. Quaternary Science Reviews, 29, 2518–2543,
1427 2010.
- 1428 Muzikar, P., Elmore, D., and Granger, D.E.: Accelerator mass spectrometry in geologic
1429 research. Geological Society of America Bulletin, 115, 643–654, doi: [10.1130/0016-
1430 7606\(2003\)115](https://doi.org/10.1130/0016-7606(2003)115), 2003.
- 1431 Nuriel, P., Rosenbaum, G., Zhao, J.-X., Feng, Y., Golding, S.D., Villemant, B., and
1432 Weinberger, R.: U-Th dating of striated fault planes. Geology, 40, 647–650, 2012.
- 1433 Palumbo, L., Benedetti, L., Bourlès, D., Cinque, A., and Finkel, R.: Slip history of the
1434 Magnola fault (Apennines, Central Italy) from ³⁶Cl surface exposure dating: evidence for
1435 strong earthquakes over the Holocene. Earth and Planetary Science Letters, 225, 163–
1436 176, doi: [10.1016/j.epsl.2004.06.012](https://doi.org/10.1016/j.epsl.2004.06.012), 2004.
- 1437 Papanikolaou, I.D., Roberts, G.P., Deligiannakis, G., Sakellariou, A., and Vassilakis, E.: The
1438 Sparta Fault, Southern Greece: From segmentation and tectonic geomorphology to
1439 seismic hazard mapping and time dependent probabilities. Tectonophysics, 597–598, 85–
1440 105, 2013.
- 1441 ~~Pavlidis, S. and Caputo, R.: Magnitude versus faults’ surface parameters: quantitative
1442 relationships from the Aegean Region. Tectonophysics, 380, 159–188, 2004.~~
- 1443 Pope, R.J. and Wilkinson, K.N.: Reconciling the roles of climate and tectonics in Late
1444 Quaternary fan development on the Spartan piedmont, Greece. In: A.M. Harvey, A.E.
1445 Mather, and M. Stokes, (Eds), Alluvial Fans: Geomorphology, Sedimentology,
1446 Dynamics. Geological Society, London, Special Publications, 251, 133–152. ~~The
1447 Geological Society of London~~, 2005.

- 1448 Röshoff, K. and Cosgrove, J.: Sedimentary dykes in the Oskarshamn-Västervik area. A study
1449 of the mechanism of formation. SKB Report R-02-37, 98 pp, 2002.
- 1450 Roy, C.J.: Clastic dykes of the Pikes Peak region. [Abstract](#). Geological Society of America
1451 Bulletin, 57, 1226, 1946.
- 1452 Sagy, A. and Brodsky, E.E.: Geometric and rheological asperities in an exposed fault zone.
1453 Journal of Geophysical Research, 114, B02301, [doi: 10.1029/2008JB005701](#), 2009.
- 1454 Schlagenhauf, A., Gaudemer, Y., Benedetti, L., Manighetti, I., Palumbo, L.,
1455 Schimmelpfennig, I., Finkel, R., and Pou, K.: Using *in situ* Chlorine-36 cosmonuclide to
1456 recover past earthquake histories on limestone normal fault scarps: a reappraisal of
1457 methodology and interpretations. Geophysical Journal International, 182, 36–72, [doi:](#)
1458 [10.1111/j.1365-246X.2010.04622.x](#), 2010.
- 1459 Sharma, P., Kubik, P.W., Fehn, U., Gove, H.E., Nishiizumi, K. and Elmore, D.: Development
1460 of ³⁶Cl Cl-36 Standards for AMS. Nuclear Instruments & Methods in Physics Research
1461 Section B-Beam Interactions with Materials and Atoms, 52, 410–415, [doi:](#)
1462 [10.1016/0168-583X\(90\)90447-3](#), 1990.
- 1463 Sikora, F.J. and Moore, K.P. (Eds.): Soil Test Methods from the Southeastern United States.
1464 Southern Cooperative Series Bulletin, 419, 211 p., 2014.
- 1465 Stone, J.O.: Air pressure and cosmogenic isotope production. Journal of Geophysical
1466 Research: [Solid Earth](#), 105, [B10](#), 23753–23759, 2000.
- 1467 Stone, J.O.: Terrestrial chlorine-36 production from spallation of iron. In: Abstract of 10th
1468 International Conference on Accelerator Mass Spectrometry, Berkeley, California, USA.,
1469 2005.
- 1470 Stone, J.O., Allan, G.L., Fifield, L.K., and Cresswell, R.G.: Cosmogenic chlorine-36 from
1471 calcium spallation. Geochimica et Cosmochimica Acta, 60, 679–692, [doi: 10.1016/0016-](#)
1472 [7037\(95\)00429-7](#), 1996.
- 1473 [Stuut, J.-B., Smalley, I., and O’Hara-Dhand, K.: Aeolian dust in Europe: African sources and](#)
1474 [European deposits. Quaternary International, 198, 234–245, 2009.](#)
- 1475 [Styllas, M., Pennos, C., Persoiu, A., Godelitsas, A., Papadopoulou, L., Aidona, E.,](#)
1476 [Kantiranis, N., Ducea, M.N., Ghilardi, M., and Demory, F.: Aeolian dust accretion](#)
1477 [outpaces erosion in the formation of Mediterranean alpine soils. New evidence from the](#)
1478 [periglacial zone of Mount Olympus, Greece. Earth Surface Processes and Landforms, 48,](#)
1479 [13003–30219. DOI: 10.1002/esp.5669, 2023.](#)
- 1480 Takahashi, Y., Chatellier, X., Hattori, K.H., Kato, K., and Fortin, D.: Adsorption of rare earth
1481 elements onto bacterial cell walls and its implication for REE sorption onto natural
1482 microbial mats. Chemical Geology, 219, 53–67, 2005.
- 1483 Tesson, J., Pace, B., Benedetti, L., Visini, F., Delli Roccoli, M., Arnold, M., Aumaître, G.,
1484 Bourlès, D.L., and Keddadouche, K.: Seismic slip history of the Pizzalto fault (central
1485 Apennines, Italy) using *in situ*-produced ³⁶Cl cosmic ray exposure dating and rare earth
1486 element concentrations. Journal of Geophysical Research: Solid Earth, 121, 1983–2003,
1487 [doi:10.1002/2015JB012565](#), 2016.
- 1488 [Tikhomirov D., Amiri, N.M., Ivy-Ochs, S., Alfimov, V., Vockenhuber, C., Akçar, N.: Fault](#)
1489 [Scarp Dating Tool – a MATLAB code for fault scarp dating using in-situ chlorine-36](#)
1490 [supplemented with datasets of Yavansu and Kalafat faults. Data in brief, 26, 104476, -et](#)
1491 [al., 2019.](#)
- 1492 [Tesson, J. and Benedetti, L.: Seismic history from in situ ³⁶Cl cosmogenic nuclide data on](#)
1493 [limestone fault scarps using Bayesian reversible jump Markov chain Monte Carlo.](#)
1494 [Quaternary Geochronology, 52, 1–20, 2019.](#)

- 1495 [Tucker, G. E., McCoy, S. W., Whittaker, A. C., Roberts, G. P., Lancaster, S. T. and Phillips,](#)
1496 [R.: Geomorphic significance of postglacial bedrock scarps on normal-fault footwalls.](#)
1497 [Journal of Geophysical Research: Solid Earth, 116, F01022, 2011.](#)
- 1498 [Wallace, R. E.: Grouping and migration of surface faulting and variations in slip rates on](#)
1499 [faults in the Great Basin province. Bulletin of the Seismological Society of America, 77,](#)
1500 [868–876, 1987.](#)
- 1501 Woodcock, N.H. and Mort, K.: Classification of fault breccias and related fault rocks.
1502 Geological Magazine, 145, 435–440, [doi:10.1017/S0016756808004883](#), 2008.
- 1503 [Yang, X., Liu, Y., Li, C., Song, Y., Zhu, H., and Jin, X.: Rare earth elements of aeolian](#)
1504 [deposits in Northern China and their implications for determining the provenance of dust](#)
1505 [storms in Beijing. Geomorphology, 87, 365–377, 2007.](#)
- 1506 Zreda, M. and Noller, J. S.: Ages of prehistoric earthquakes revealed by cosmogenic
1507 chlorine-36 in a bedrock fault scarp at Hebgen Lake. Science, 282, 1097–1099, 1998.

1508 **Table 1: Parameters used to give best fits of modelled profiles to measured ³⁶Cl**
 1509 **concentration profiles, following Schlagenhauf et al. (2010), for MCMC modelling of slip**

Profile	α (°)	β (°)	γ (°)	Scarp (cm)	ρ_{rock} (g cm ⁻³)	$\rho_{colluvium}$ (g cm ⁻³)	³⁶ Cl P ₀ (at. g ⁻¹ yr ⁻¹)	ϵ (mm yr ⁻¹)	Pre (yr)	Age (kyr B.P.)	Slip (cm)	RMSw	AICc	χ^2_{red}
Fig. 3a	42	64	20	730	2.65	1.95	59.4	0.02	10-300	5.98 ± 0.4, 3.8 ± 0.3, 3.2 ± 0.3, 2.8 ± 0.2, 2.3 ± 0.2	140, 120, 130, 120, 140	10	859	3
Fig. 3b	49	64	20	730	2.65	2.04	59.4	0.02	3-900	2.5 ± 0.2, 2.3 ± 0.2	60, 140	5	406	2
Fig. 3c	42	64	20	742	2.65	1.95	59.4	0.02	12-000	8.6 ± 0.6, 5.8 ± 0.4, 3.8 ± 0.3, 3.2 ± 0.3, 2.5 ± 0.3	140, 120, 130, 120, 140	10	1338	7
Fig. 3d	42	64	20	730	2.65	1.95	59.4	0.02	10-300	5.9 ± 0.4, 3.0 ± 0.3, 2.8 ± 0.2, 1.9 ± 0.2	240, 140, 180, 80	12	875	5

1510 rate.

α (°)	β (°)	γ (°)	Scarp (cm)	Buried scarp (cm)	ρ_{rock} (g cm ⁻³)	$\rho_{colluvium}$ (g cm ⁻³)	³⁶ Cl P ₀ (at. g ⁻¹ yr ⁻¹)	ϵ (mm yr ⁻¹)	Pre (kyr)	Scarp age (kyr ± 1σ)	Elapsed time (kyr ± 1σ)
32	62	20	650	80	2.6	1.9	59.4 ± 4.3	0.02	7.7	8.0 ± 1.5	2.5 ± 1.0

1511

1512 α is hanging wall colluvial surface dip angle; β is scarp dip angle; γ is the dip angle of the hillslope above the fault scarp; ϵ is
 1513 scarp erosion rate; Pre is pre-exposure; Scarp age is the initial estimate of exhumation of the oldest (highest) part of the
 1514 scarp; Elapsed time is the estimated duration following the last earthquake, inferred earthquake age(s) with 0 inserted to model
 1515 scarp samples from below the surface of the hanging wall colluvium; Slip is the inferred displacement for each earthquake. On
 1516 each profile, the oldest age and associated displacement, shown in grey, are fitted to the top of the vertical sample transect
 1517 rather than fitted to a step in ³⁶Cl concentration; RMSw is weighted root mean square; AICc is Akaike Information Criterion; χ^2_{red}
 1518 is reduced Chi-square. Model best fits for each data set are shown in black. The ³⁶Cl production rate of 59.4 ± 4.3 at g⁻¹ yr⁻¹ is
 1519 taken from Schlagenhauf et al. (2010), calculated from Lifton et al. (2005).
 1520 When using the ³⁶Cl production rate of 48.8 ± 3.5 at g⁻¹ yr⁻¹ from Stone et al. (1996), Pre is 10.6 kyr; otherwise, all other
 1521 parameters are fixed.

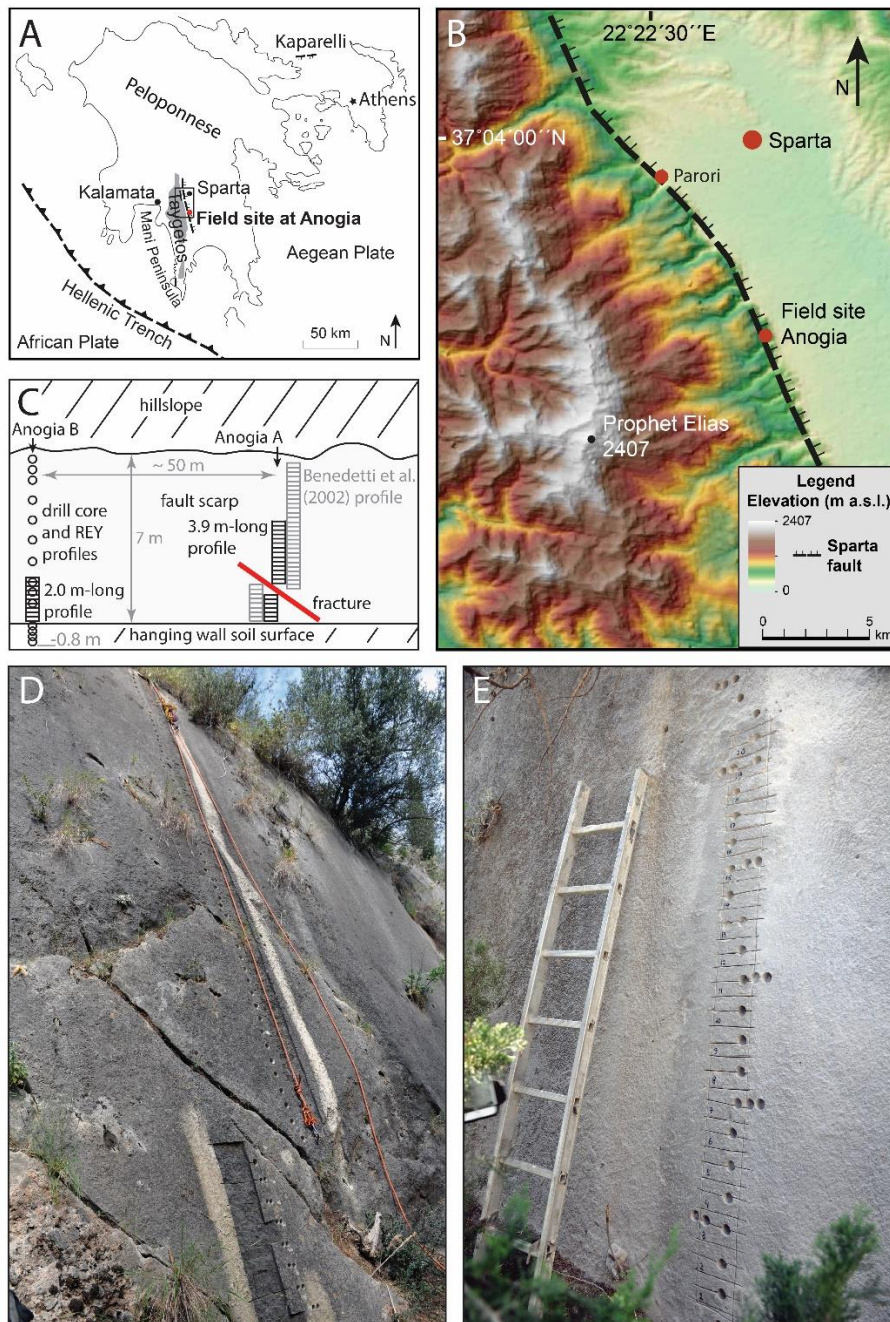
1522

1523 **Table 2: Slip rates for the Sparta fault at Anogia from the best Markov chain Monte Carlo**
 1524 **models (n = 10,000), for end-member ³⁶Cl production rates and varying number of model**
 1525 **earthquakes.**

Slip rate calculation model (³⁶ Cl production rate, number of earthquakes)	Mean slip rate (mm yr ⁻¹)	MAP slip rate (mm yr ⁻¹)
48.8, 3 earthquakes, to present	0.72	0.70
48.8, 5 earthquakes, to present	0.71	0.70
48.8, 6 earthquakes, to present	0.70	0.70
59.4, 3 earthquakes, to present	0.79	0.76
59.4, 5 earthquakes, to present	0.78	0.75
59.4, 6 earthquakes, to present	0.77	0.75
48.8, 3 earthquakes, to 464 B.C.E. earthquake	1.10	1.08
48.8, 5 earthquakes, to 464 B.C.E. earthquake	1.11	1.11
48.8, 6 earthquakes, to 464 B.C.E. earthquake	1.10	1.11
59.4, 3 earthquakes, to 464 B.C.E. earthquake	1.21	1.15
59.4, 5 earthquakes, to 464 B.C.E. earthquake	1.22	1.16
59.4, 6 earthquakes, to 464 B.C.E. earthquake	1.22	1.18
48.8, 5 earthquakes, 0–3.74.9 m on fault scarp	0.951.08	0.941.05
59.4, 5 earthquakes, 0–3.74.9 m on fault scarp	1.0348	0.964.23
48.8, 5 earthquakes, 3.74.9–6.5 m on fault scarp	0.8376	0.80
59.4, 5 earthquakes, 3.74.9–6.5 m on fault scarp	0.92	0.92

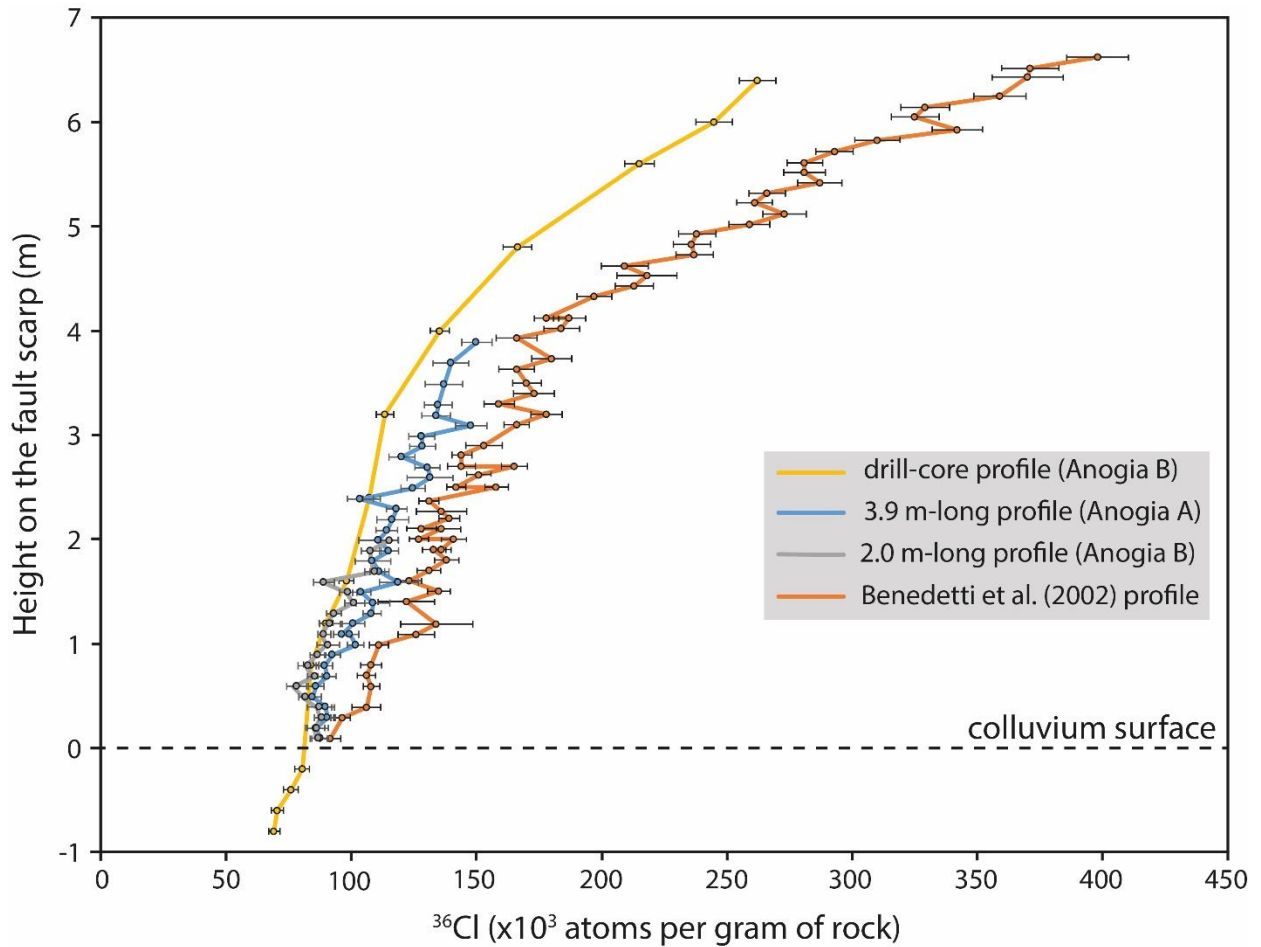
1526

MAP is maximum a posteriori probability



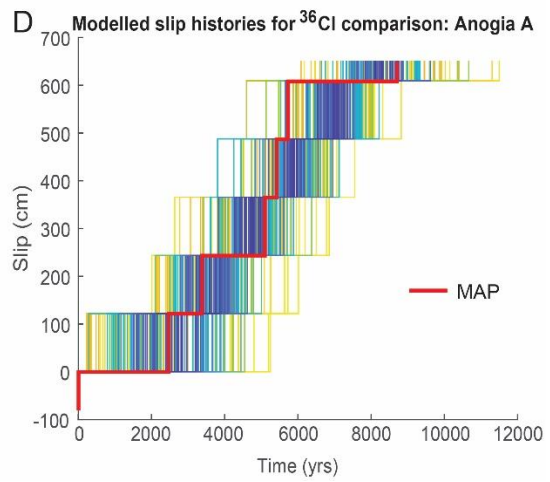
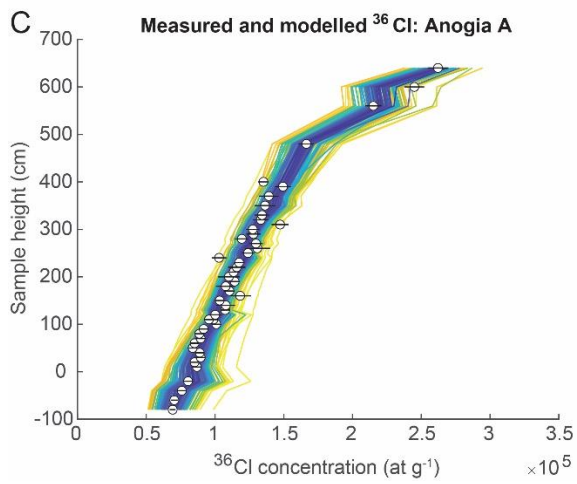
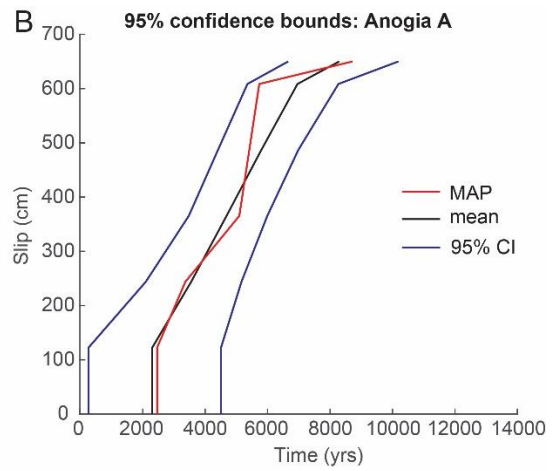
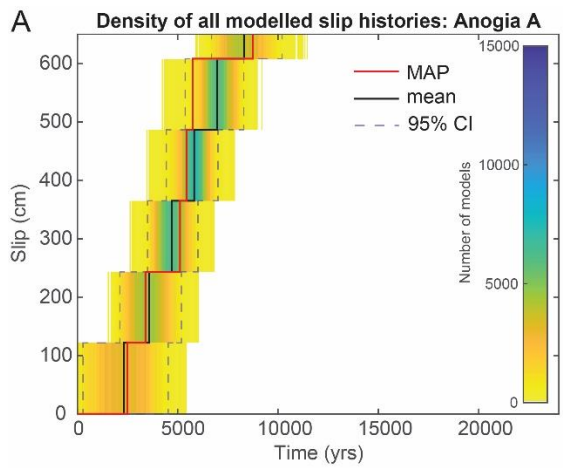
1528

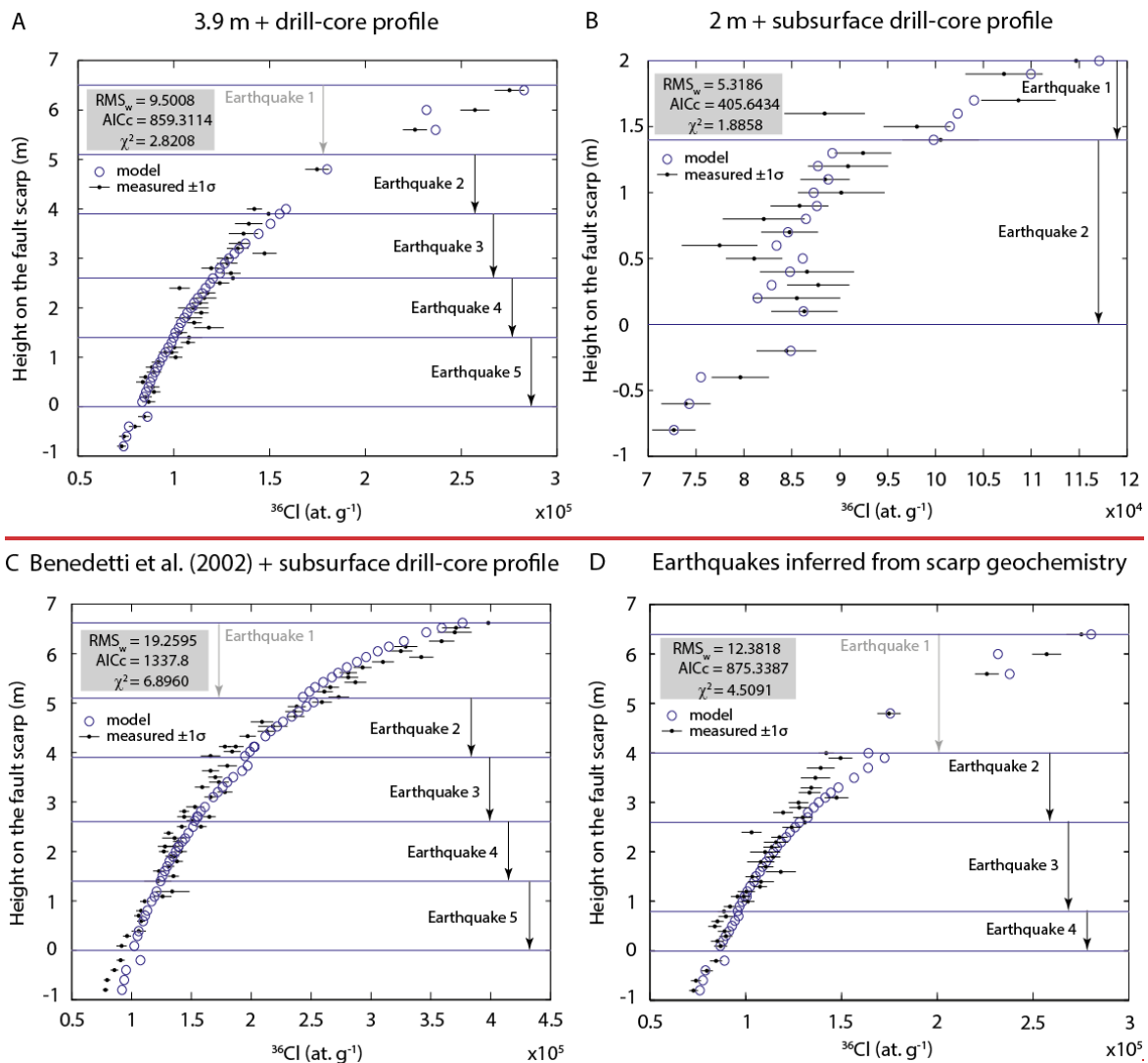
1529 **Fig. 1:** Study site. A. The study site location in Peloponnese, Greece. Key tectonic features
 1530 are shown. Box indicates location of panel B. B. The location of the Sparta fault, separating
 1531 the Taygetos Mountains from the Sparta basin. The location of the Anogia field site used both
 1532 in this study and in Benedetti et al. (2002) is shown. Benedetti et al. (2002) located a second
 1533 sampling transect at Parori (also shown). The digital elevation model has a 24 m resolution
 1534 and is derived from ASTER GDEM (GDEM2), which is a product of NASA and METI
 1535 (Japan). C. Schematic diagram of the Sparta fault scarp at Anogia, showing the locations of
 1536 our vertical ^{36}Cl and **REYREE-Y** sampling transects, and the ^{36}Cl sampling transect of
 1537 Benedetti et al. (2002). D. Photograph showing the location of our 3.9 m-long profile, prior to
 1538 sampling. The existing sample scar is from Benedetti et al. (2002). E. Photograph showing
 1539 the location of our **REYREE-Y** and drill core profiles, after sampling, and our 2.0 m long
 1540 profile, before sampling.



1541
 1542
 1543
 1544
 1545
 1546
 1547
 1548
 1549
 1550

Fig. 2: Sparta fault ^{36}Cl concentration profiles. Error bars indicate 1σ measurement uncertainties. ~~Time averaged uplift rates inferred from profile gradients are shown in grey. For the lower, more recently exposed, parts of the scarp surface, uplift rates are calculated for time starting from the present day. If uplift rates are alternatively calculated as occurring prior to the subaerial exposure of the lowermost samples by the most recent earthquake, cumulative uplift rates increase to 2.8 mm yr^{-1} and 1.8 mm yr^{-1} for the lower parts of the 3.9 m long and Benedetti et al. (2002) profiles, respectively.~~



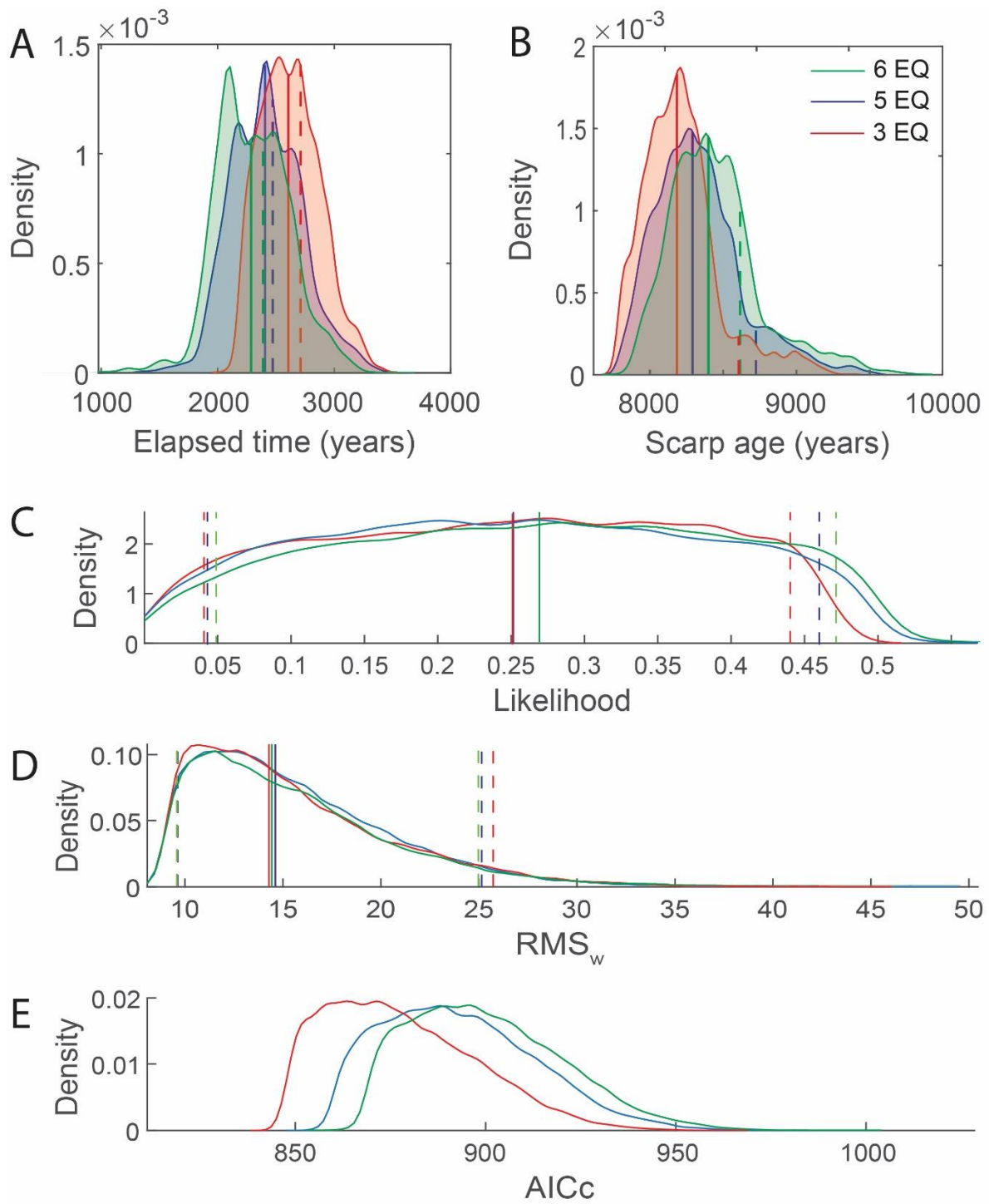


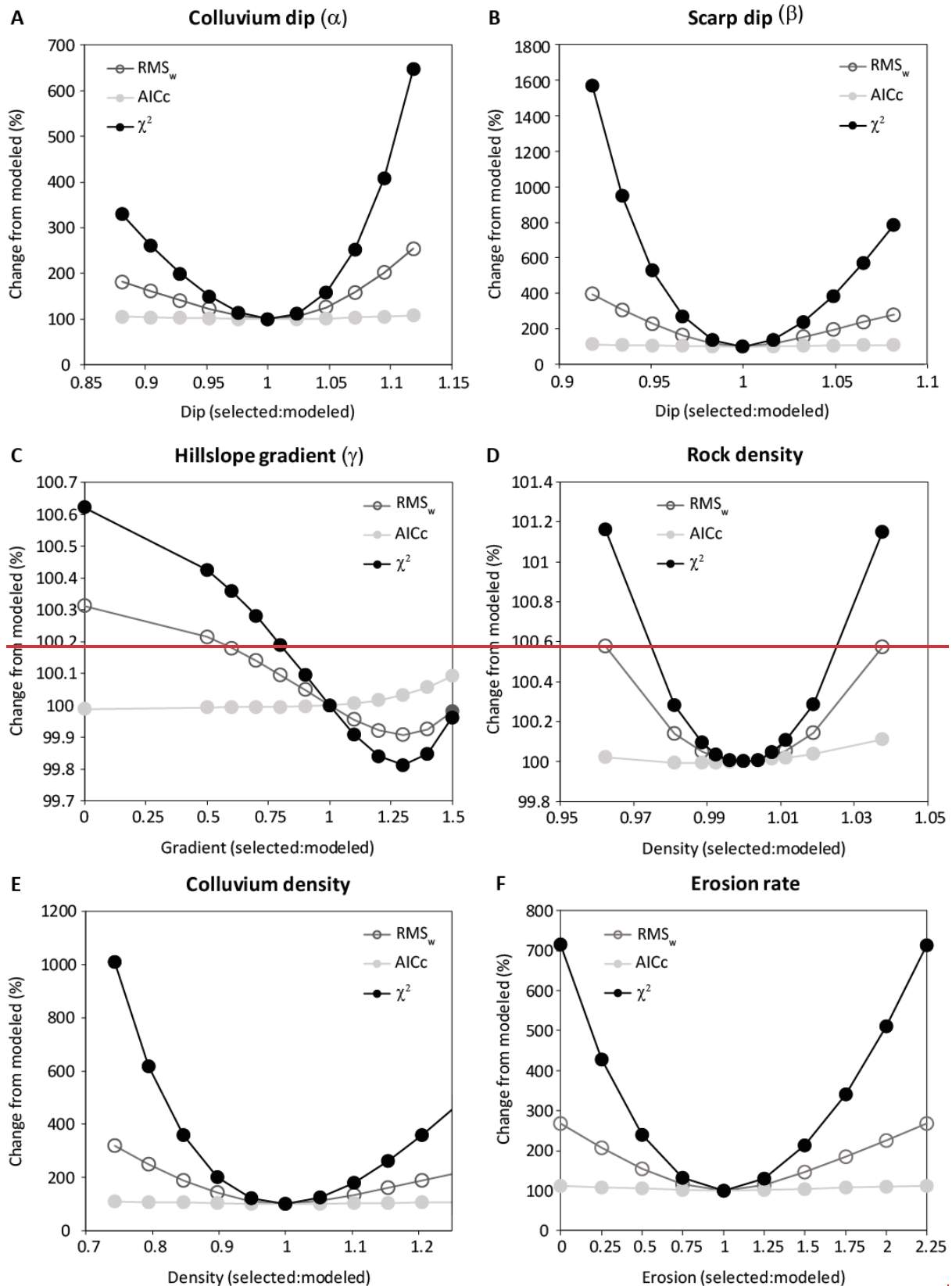
1552
1553
1554
1555
1556
1557
1558
1559
1560
1561
1562
1563
1564
1565
1566
1567
1568
1569

Fig. 3: Markov chain Monte Carlo (MCMC) model fits to measured ^{36}Cl concentrations and model slip histories, Anogia A + drill core profile. Slip accumulation is shown for five model earthquakes that each exhume the same vertical length of scarp rather than reflecting the magnitude and timing of historical earthquakes. The red line in panels a, b, and d is the maximum a posteriori probability (MAP) estimation model, which is the maximum likelihood multiplied by the prior probability based on scarp age. Each panel includes 160k iterations, following removal of a burn-in of the first 40k iterations. A. Histogram showing the distribution of accepted model slip histories in slip-space versus time. The density of overlapping models increases from warm to cool colours. The mean model and 95% confidence bounds are also shown. B. The 95% confidence bounds of the smoothed model distribution (black lines) calculated for age at each step in the slip. The mean (black line) and MAP (red line) slip histories are also plotted. C. Model fits to measured ^{36}Cl concentrations (circles). The coloured lines represent a selection of 160 model fits from low- (yellow) to high-probability (blue) at equal intervals (1000) through the distribution. The black lines indicate 1σ measurement uncertainties. D. Slip histories through five model earthquakes corresponding to MCMC fits shown in panel c. Results are shown for a ^{36}Cl production rate

1570 of 59.4 ± 4.3 atoms g Ca⁻¹ yr⁻¹. Refer to Fig. S2 for equivalent results using a production rate
1571 of 48.8 ± 3.5 atoms g Ca⁻¹ yr⁻¹.

1572 **Fig. 3:** Best fits of profiles modelled according to Schlagenhauf et al. (2010) to measured
1573 Sparta fault ³⁶Cl concentration profiles. Down arrows indicate the section of scarp exhumed
1574 during each earthquake. Best fits of modelled profiles to measured data are indicated by
1575 lowest attainable values for each of RMS_w , χ^2_{red} , and AICc. A. Anogia 3.9 m profile plus drill
1576 core profile data above 3.9 m and below the present hanging wall colluvium surface. B.
1577 Anogia 2.0 m profile plus drill core profile data from below the present hanging wall
1578 colluvium surface. C. Benedetti et al. (2002) data, remodeled using the same parameters as
1579 for panel A. The modelled profile is smooth because scarp composition is based on a mean
1580 value taken from our data. Our drill core subsurface samples were also used to help remodel
1581 the Benedetti et al. (2002) data, which required adding 13% on to their measured
1582 concentrations. D. Same profile as in A but with earthquakes inferred from the fault scarp
1583 geochemistry.





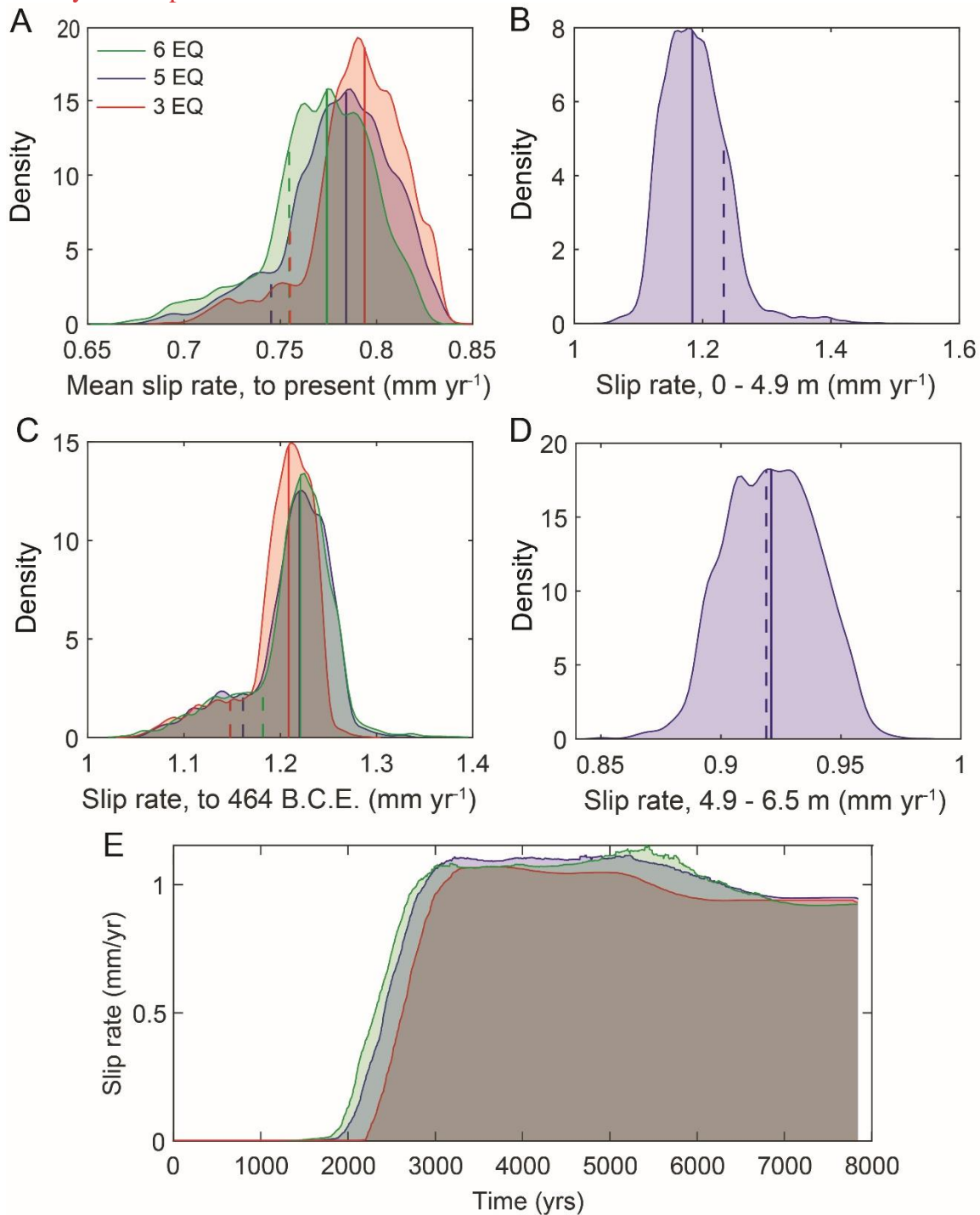
1585
 1586
 1587
 1588
 1589
 1590

Fig. 4: Statistical plots for 160k Markov chain Monte Carlo (MCMC) model iterations, following removal of a 40k burn-in. Results are shown for three, five, and six model earthquakes. Vertical red lines indicate the median of each distribution, whereas vertical green lines indicate 95% confidence intervals. Posterior probability distribution functions from all models for A. Elapsed Time, and B. Scarp Age. Distributions of C. Likelihood, D.

1591 [Weighted mean root square \(RMS_w\)](#), and [E. Ceorrected Akaike's Information Criterion](#)
1592 [\(AICc\)](#) of slip history calculated for modelled ³⁶Cl concentrations compared to the measured
1593 [values](#).

1594

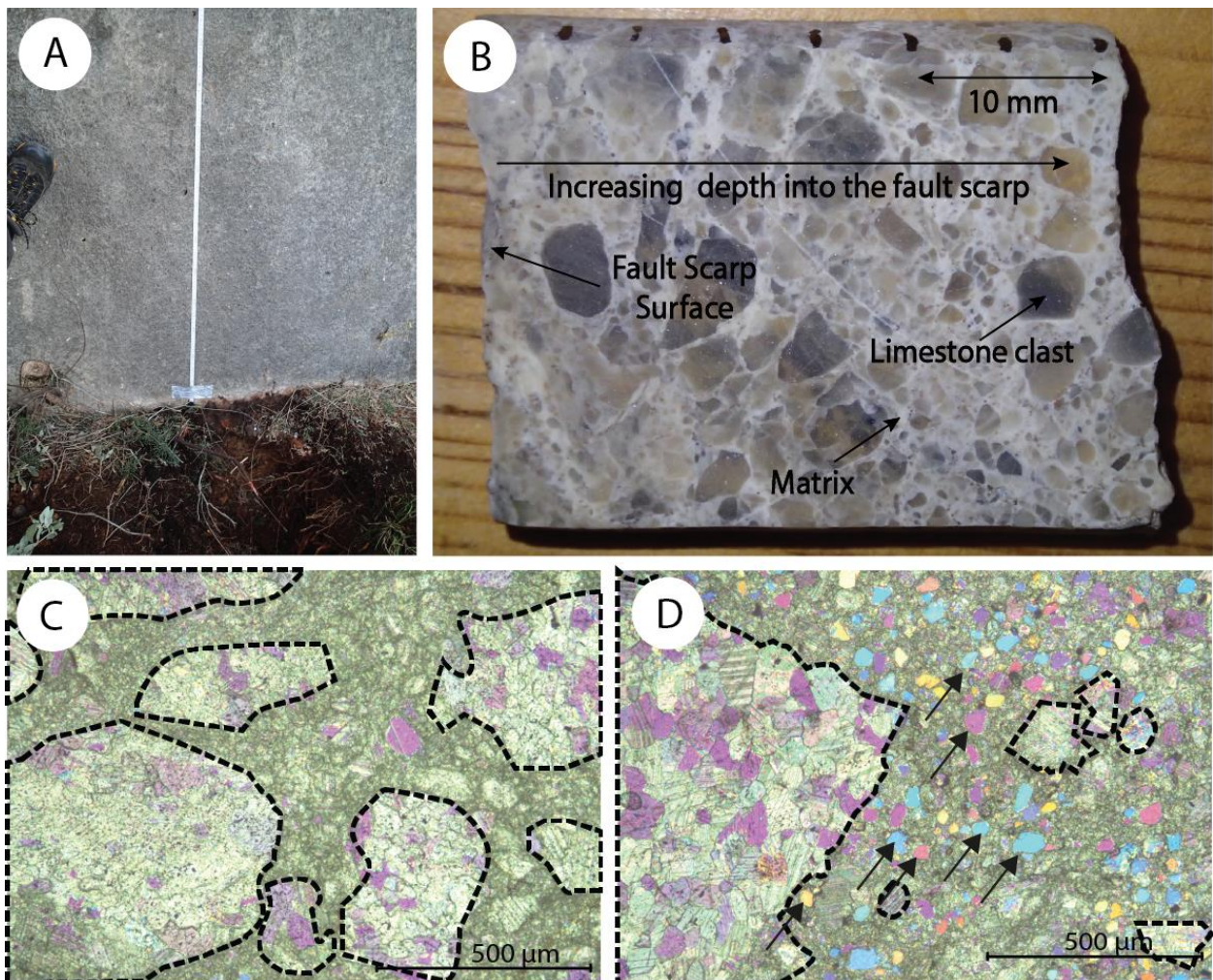
1595 **Fig. 4:** Sensitivity of fits of profiles modelled according to Schlagenhauf et al. (2010) to
1596 measured Sparta fault ³⁶Cl concentration profiles, according to input parameters. A. Colluvial
1597 wedge dip B. Scarp dip C. Slope angle above the scarp. D. Scarp rock density E. Colluvium
1598 density F. Scarp erosion rate.



1599

1600
1601
1602
1603
1604
1605
1606
1607
1608
1609
1610
1611
1612
1613

Fig. 5: Slip rates for the Sparta fault at Anogia (Anogia A plus drill core profile) from Markov chain Monte Carlo modelling. Results are shown for three, five, and six model earthquakes. In each panel, the most probable (top 10%) models calculated from the median scarp age and scarp height are shown. Solid and dashed vertical lines indicate the mean and maximum a posteriori probability (MAP) estimation for each distribution, respectively. Slip rates are shown for three, five, and six model earthquakes, using a ^{36}Cl production rate of 59.4 ± 4.3 atoms $\text{g Ca}^{-1} \text{yr}^{-1}$. A. The distribution of the most probable slip rate for the entire scarp calculated up to the present day. B. The distribution of the most probable slip rate for the entire scarp calculated up to the last known earthquake at 464 B.C.E. C. The distribution of the most probable slip rate for lower segment of the scarp. D. The distribution of the most probable slip rate for the uppermost segment of the fault scarp. E. Mean slip rate over time. Slip rates using a ^{36}Cl production rate of 48.8 ± 3.5 atoms $\text{g Ca}^{-1} \text{yr}^{-1}$ are shown in Fig. S2.

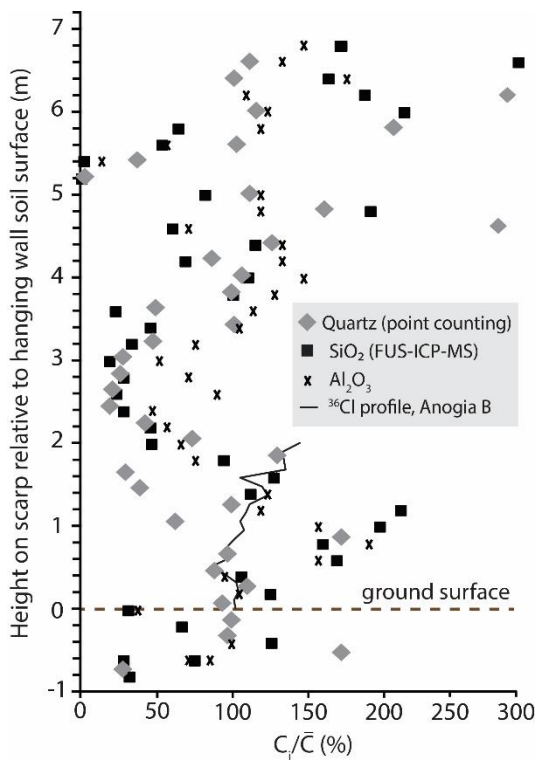


1614

Fig. 56: The heterogeneous fault breccia that comprises the Sparta fault scarp surface. A. The Sparta fault scarp surface appears smooth and homogenous, as illustrated by this photograph of the scarp base at Anogia (upper half of the dug trench in the foreground). B. Fault breccia is revealed in a cut drill core, where clasts of host limestone are cemented in a fine matrix. C. A photomicrograph shows limestone clasts (dotted outlines) comprising about 60% of the

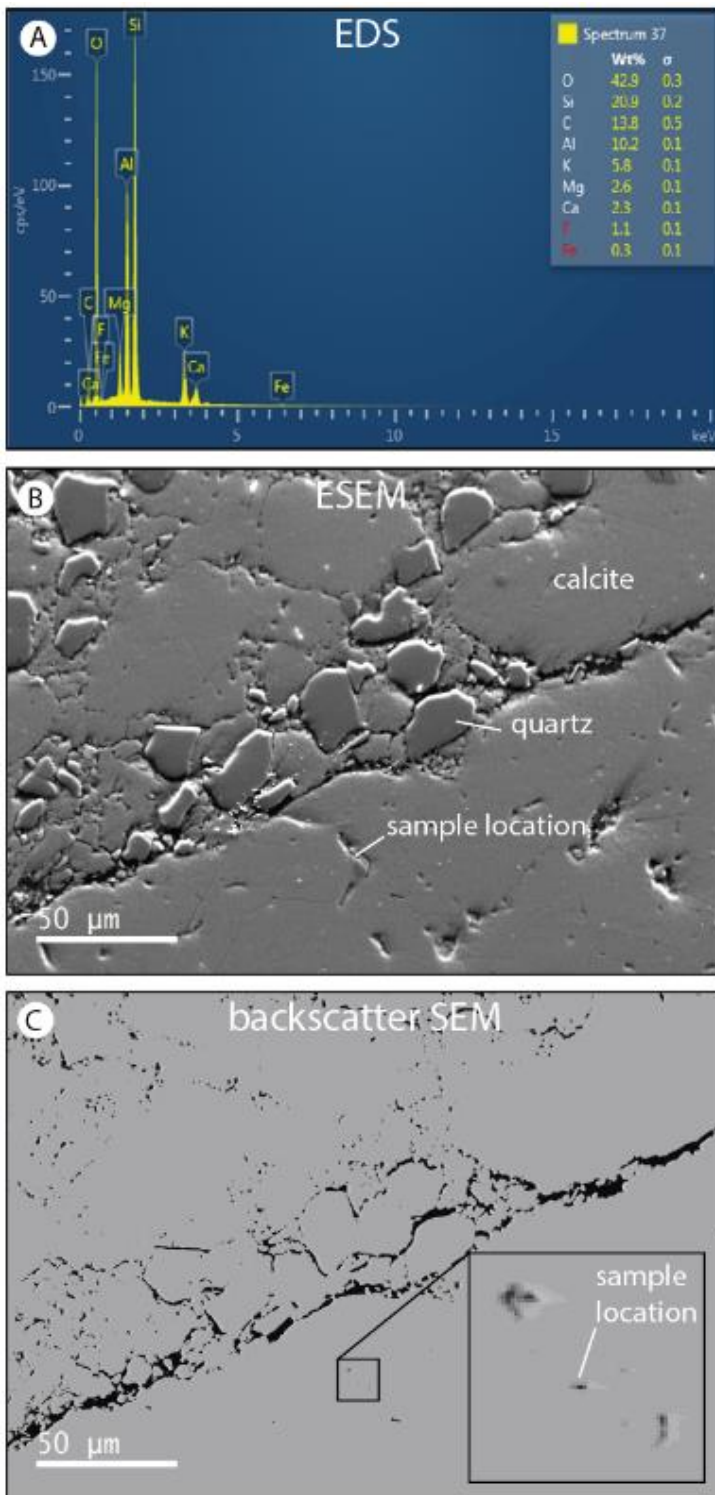
1620 thin section area. D. A photomicrograph shows fine matrix comprising about 60% of the thin
1621 section area. Arrows indicate quartz.

1622

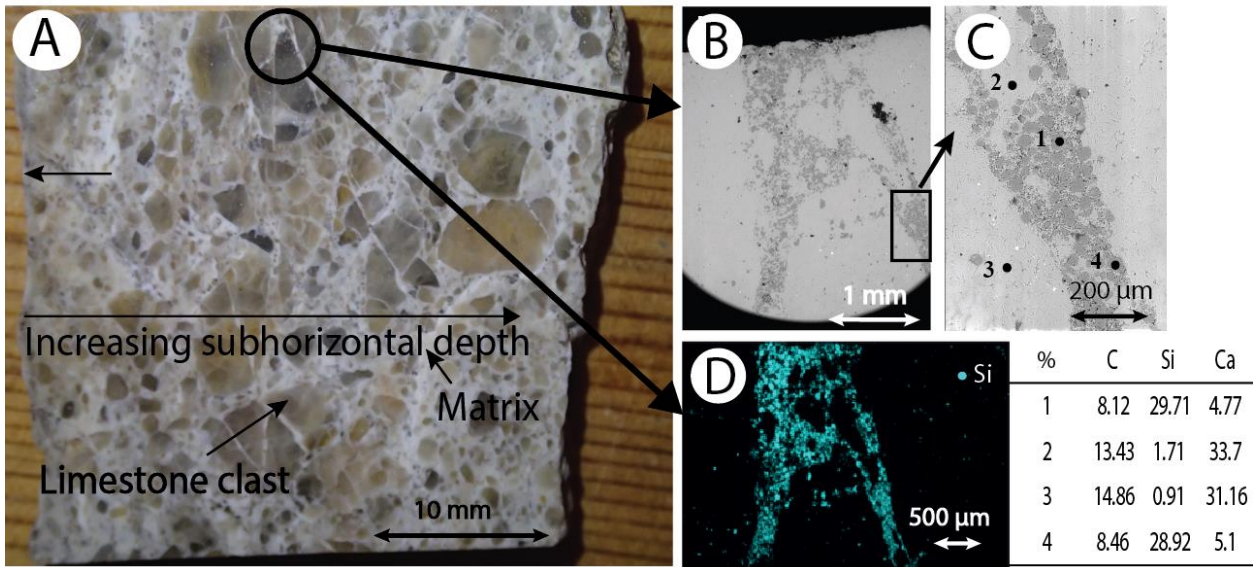


1623

1624 **Fig. 67:** Concentrations of Al₂O₃ and SiO₂, and quartz abundances from point counting,
1625 along a vertical profile, Sparta fault scarp, Anogia. The concentration of each element (C_i) is
1626 normalized to its mean concentration through the profile (C_i/\bar{C}). The locations of former soil
1627 surface horizons inferred from ³⁶Cl concentrations and from the scarp geochemistry are
1628 shown for reference.

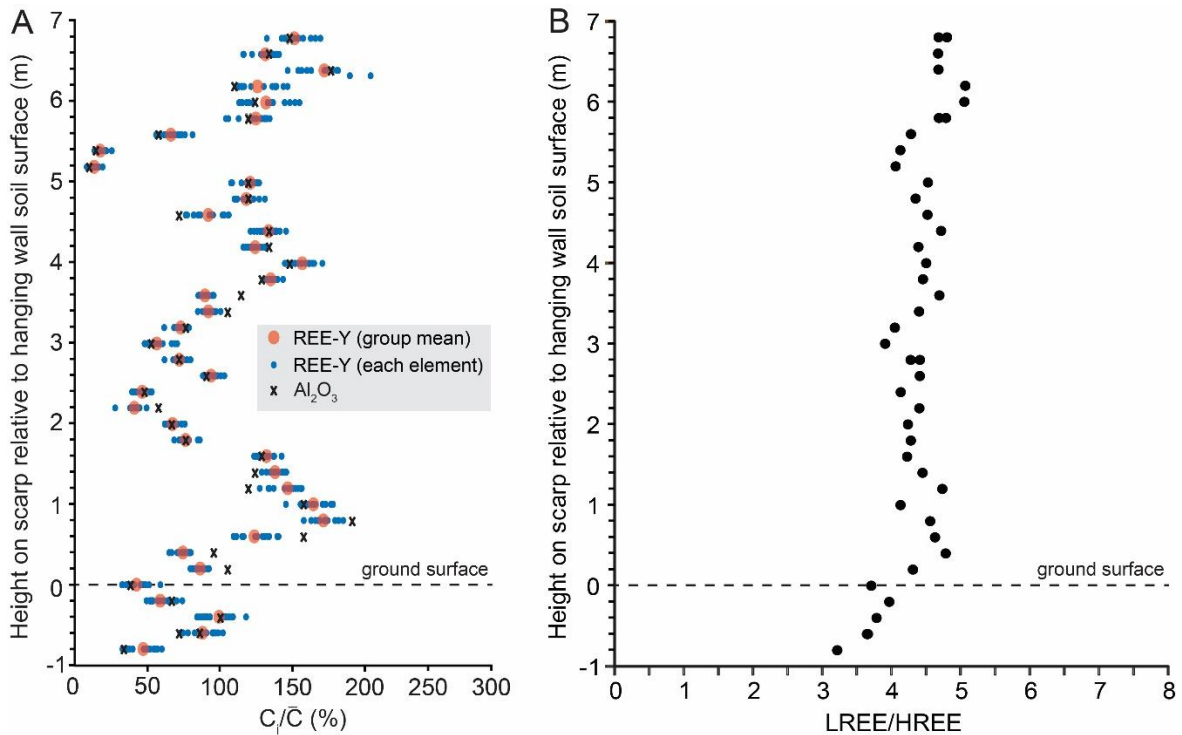


1629
 1630 **Fig. 78:** Energy-dispersive X-ray spectroscopy (EDS) elemental abundances, and
 1631 environmental scanning electron microscope (ESEM) and backscatter SEM imagery of a thin
 1632 section of fault breccia comprising the Sparta fault scarp surface at 1.1 m above the hanging
 1633 wall. (A). Element abundances in a pore, the location of which is shown in panels B and C.
 1634 Si, Al, and K are abundant relative to Ca, which indicates that clay, e.g., illite, is lining the
 1635 pore. (B) Quartz is an abundant constituent of the thin section matrix. (C) Porosity, shown in
 1636 black; note its spatial association with quartz. The location of the sample used in panel A is in
 1637 a small pore, shown in the inset.



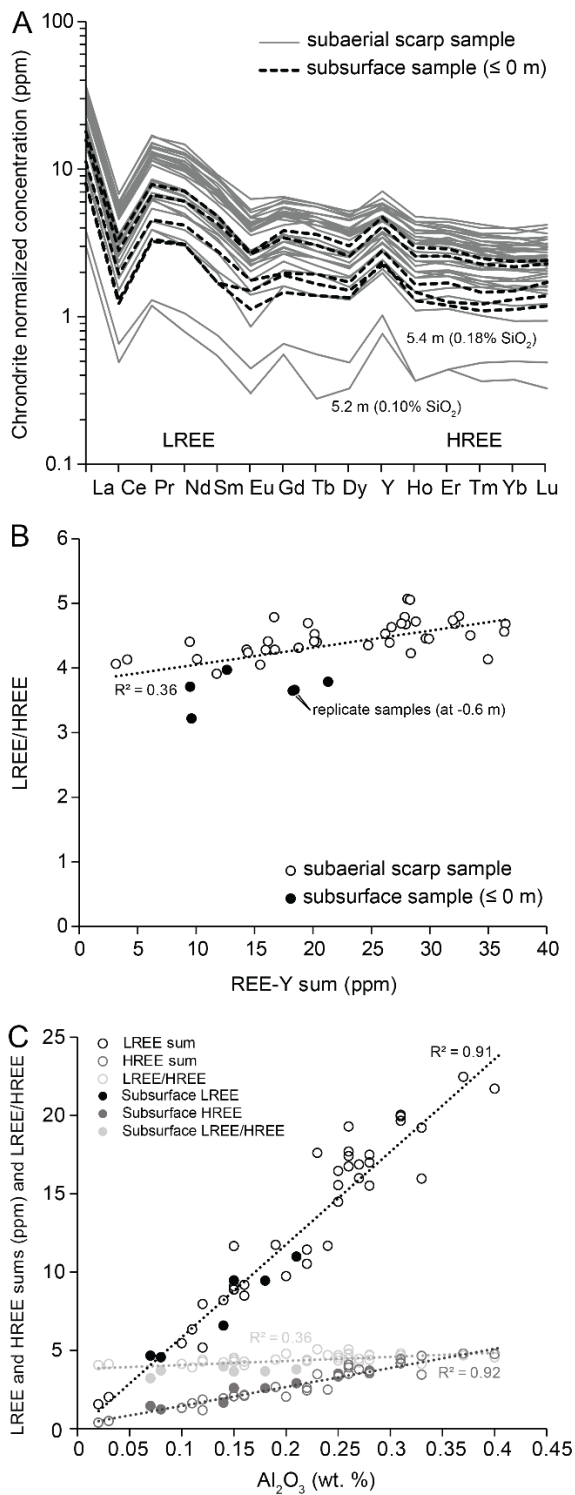
1639 **Fig. 89:** Concentrations of Si in the Sparta fault breccia, 1.1 m above the scarp base at
 1640 Anogia. A. A cut drill core from the Sparta fault scarp at Anogia showing limestone clasts
 1641 cemented in fine matrix. The circled fine matrix is examined under high resolution in panels
 1642 B to D. B. An ESEM image showing the sample location for spot elemental analysis
 1643 (rectangle). C. Sample points for elemental analysis using EDS, with values shown in the
 1644 table. D. The abundance of Si in the fine matrix illustrated in magenta for the circled part of
 1645 the thin section shown in panel A.

1647



1648 A
 1649 B

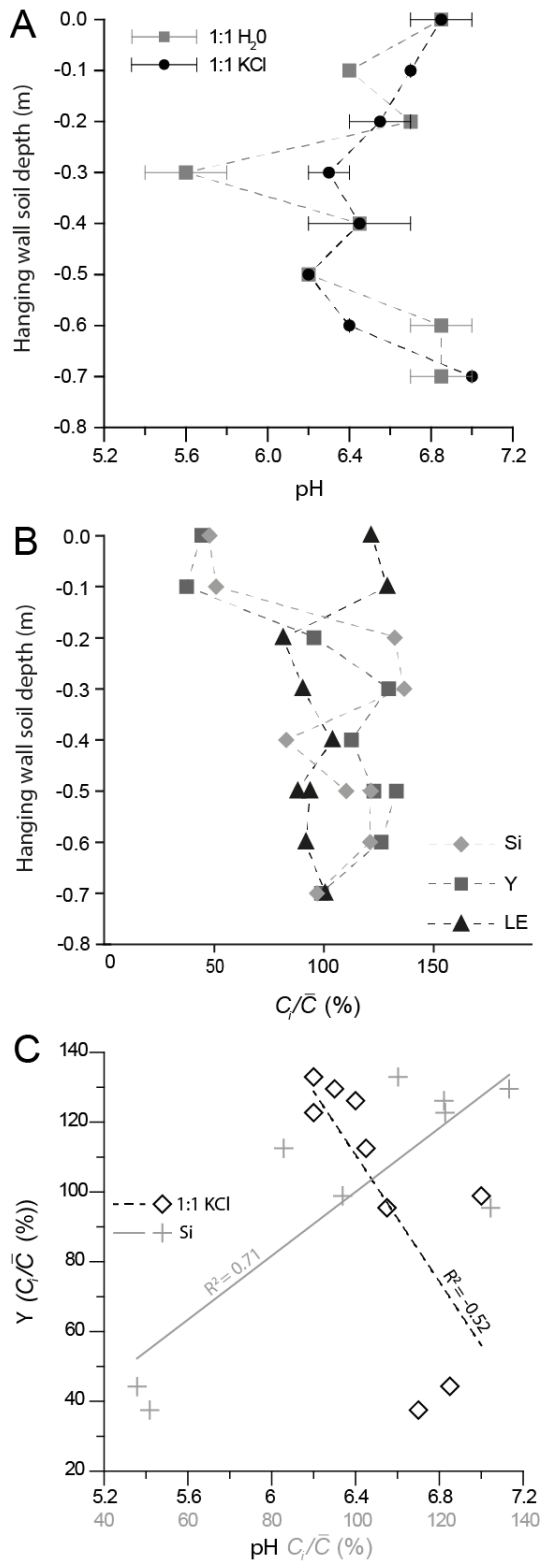
1650 **Fig. 910:** Vertical distribution of REE-Y elements on the Sparta fault (Anogia B profile). A.
1651 Concentrations of rare earth elements and yttrium (REYREE-Y concentrations.) along a
1652 vertical profile on the Sparta fault at Anogia. Mean values for all REYREE-Y elements at
1653 each sample point are shown in red dots, whereas individual REYREE-Y elements are shown
1654 in blue dots. The concentration of each element (C_i) is normalized to its mean concentration
1655 through the profile (C_i/\bar{C}). Concentrations of Al_2O_3 and former soil surface horizons inferred
1656 from ^{36}Cl concentrations profiles and geochemical data, are shown for reference. B.
1657 LREE:HREE ratio. There are two measurements at -0.6 m.
1658
1659
1660



1661
1662
1663
1664
1665
1666
1667
1668
1669

Fig. 1011: REE-Y elements on the Sparta fault (Anogia B profile). **A.** Concentrations of rare-earth elements and yttrium (REYREE-Y) normalized to chondrite composition (McDonough and Sun, 1995) for the Sparta Fault scarp at Anogia. Each line shows a measured location on the scarp surface. The two low REYREE-Y outliers at 5.2 m and 5.4 m also have exceptionally low SiO_2 and Al_2O_3 . **B.** LREE:HREE versus REE-Y sum. The R^2 value is for a linear fit. **C.** LREE, HREE, and LREE:HREE versus Al_2O_3 (wt.%). The R^2 values are for linear fits. In each panel, the six subsurface samples (≤ 0 m), including a replicate measurement at -0.6 m.

1670



1671
1672
1673
1674
1675
1676
1677
1678

Fig. 412: Hanging wall soil chemistry, adjacent to the Sparta fault scarp at Anogia. A. Soil pH along a vertical profile measured from soil mixed with distilled H₂O and 1M KCl. Uncertainty ranges show the ≤ 0.5 resolution of the indicator strips. B. Concentrations of Si, Y, and elements too light to be measured using handheld XRF (LE, including C) along the vertical soil profile. Each element has been normalized through division by its mean concentration through the soil. C. Y concentrations plotted against pH (measured from 1:1 KCl) and Si concentration at each measured depth interval beneath the soil surface.